

# Tensor part of the Skyrme energy density functional.

## II: Deformation properties of magic and semi-magic nuclei

M. Bender,<sup>1,2</sup> K. Bennaceur,<sup>3</sup> T. Duguet,<sup>4,5</sup> P.-H. Heenen,<sup>6</sup> T. Lesinski,<sup>3,7,8</sup> and J. Meyer<sup>3</sup>

<sup>1</sup>*Université Bordeaux, Centre d'Etudes Nucléaires de Bordeaux Gradignan, UMR5797, F-33175 Gradignan, France*

<sup>2</sup>*CNRS/IN2P3, Centre d'Etudes Nucléaires de Bordeaux Gradignan, UMR5797, F-33175 Gradignan, France*

<sup>3</sup>*Université de Lyon, F-69003 Lyon, France; Institut de Physique Nucléaire de Lyon,*

*CNRS/IN2P3, Université Lyon 1, F-69622 Villeurbanne Cedex, France*

<sup>4</sup>*CEA, Irfu, SPhN, Centre de Saclay, F-911191 Gif-sur-Yvette, France*

<sup>5</sup>*National Superconducting Cyclotron Laboratory and Department of Physics and Astronomy, Michigan State University, East Lansing, MI 48824, USA*

<sup>6</sup>*PNTPM, CP229, Université Libre de Bruxelles, B-1050 Bruxelles, Belgium*

<sup>7</sup>*Department of Physics and Astronomy, University of Tennessee, Knoxville, TN 37996, USA*

<sup>8</sup>*Physics Division, Oak Ridge National Laboratory, Oak Ridge, TN 37831, USA*

(Dated: 20 September 2009)

We study systematically the impact of the time-even tensor terms of the Skyrme energy density functional, i.e. terms bilinear in the spin-current tensor density, on deformation properties of closed shell nuclei corresponding to 20, 28, 40, 50, 82, and 126 neutron or proton shell closures. We compare results obtained with three different families of Skyrme parameterizations whose tensor terms have been adjusted on properties of spherical nuclei: (i)  $TIJ$  interactions proposed in the first paper of this series [T. Lesinski *et al.*, Phys. Rev. C **76**, 014312 (2007)] which were constructed through a complete readjustment of the rest of the functional (ii) parameterizations whose tensor terms have been added perturbatively to existing Skyrme interactions, with or without readjusting the spin-orbit coupling constant. We analyse in detail the mechanisms at play behind the impact of tensor terms on deformation properties and how studying the latter can help screen out unrealistic parameterizations. It is expected that findings of the present paper are to a large extent independent of remaining deficiencies of the central and spin-orbit interactions, and will be of great value for the construction of future, improved energy functionals.

PACS numbers: 21.30.Fe; 21.10.Dr; 21.10.Pc; 21.60.Jz

### I. INTRODUCTION

Our experimental knowledge of the evolution of shell structure in atomic nuclei as a function of proton and neutron numbers has largely increased over the last few years. The difficulty to describe these new results has triggered the search for mechanisms that could alter nuclear shell structure when going toward unstable nuclides and approaching nucleon drip lines. One such mechanism that has an impact on the shell structure of stable and unstable nuclei is provided by the tensor force between nucleons [1].

The tensor force is a key ingredient of all vacuum nucleon-nucleon interactions. It is also explicitly included in the shell-model interaction for Hamiltonians constructed from first principles. By contrast, it was absent from methods based on the introduction of a self-consistent mean-field [2], until recent studies based on the Skyrme or Gogny modeling of the in-medium strong interaction [3, 4, 5, 6, 7, 8].

The renewed interest in the residual tensor interaction is due to its very specific effect on nuclear spectra. It brings a correction to binding energies and to spin-orbit splittings that fluctuates with the filling of shells. Its introduction seems, therefore, necessary to improve the predictive power of mean-field-based methods. The Skyrme and Gogny parameterizations are viewed to-

day as nuclear energy density functionals (EDF). Their derivation from first principles is still lacking, although significant advances have been made recently for the pairing part [9]. Instead, one still has to resort to the phenomenological construction of an EDF and adjust its free parameters, including those associated with tensor terms, to data. How to perform this adjustment in an optimal manner is still an unsettled question. The main problem is to find experimental observables which can unambiguously be related to a mean-field result and are primarily sensitive to a specific part of the EDF, e.g., the tensor part. Such a link between experiment and theory is very often obscured by collective fluctuations around the mean-field states [10, 11].

The tensor contribution to single-particle energies depends on the filling of shells. It (nearly) vanishes in spin-saturated nuclei, whereas it might be significant when only one level out of two spin-orbit partners is filled. The breaking of spherical shells in deformed nuclei leads to a strong modification of the net spin saturation; hence, the contribution of the tensor force to mean fields and the total energy evolves with deformation. To the best of our knowledge, this was never studied in the published literature. The authors of Ref. [8] considered deformation, but did not study the impact of tensor terms on deformation properties as such.

In local energy density functionals of the Skyrme type, the tensor force manifests itself through terms that are

bilinear in the local pseudotensor spin-current density. In Ref. [6], referred to as Article I in what follows, the impact of these terms on the mean-field ground states of spherical nuclei was studied. In the most general case, three bilinear combinations of the pseudotensor spin-current density can be constructed from a zero-range tensor force, one of them being also generated by a momentum-dependent central zero-range two-body force. All of these terms extrapolate differently when going from spherical to deformed shapes. For the sake of simplicity, we will denote all of the three terms that are bilinear in the spin-current tensor density as *tensor terms* throughout this article, although one of them is already present as soon as a zero-range central velocity-dependent interaction is used as a starting point to derive the EDF.

A word of caution: We cannot expect to significantly improve the agreement with all experimental data, as we learned in our study of spherical nuclei that most deficiencies of the single-particle spectra predicted by standard Skyrme interactions without tensor terms persist in our fits including these terms. Indeed, one of the major results of Article I is that the current form of the *central* Skyrme interaction is not flexible enough to allow for a satisfactory description of single-particle spectra. Adding tensor terms and adjusting them tightly to very specific spectroscopic quantities often amplifies the deficiencies of the central and spin-orbit parts as currently used, which seem to establish a compromise that averages over the details of shell structure. This is consistent with the recent study of Kortelainen *et al.* [12], who point out that it seems impossible to satisfactorily describe single-particle levels of doubly-magic nuclei with a standard Skyrme energy density functional including tensor terms, even when relaxing all constraints from bulk properties.

The aim of the present study is to investigate the generic influence of the tensor terms on deformation properties. The questions to be addressed here are:

- (i) How do the tensor terms influence the topography of deformation energy curves of even-even nuclei, given their spherical shell-structure, in particular regarding the number of spin-unsaturated levels at sphericity?
- (ii) How much of these changes is caused by the tensor terms themselves, how much is caused by the rearrangement of all other terms during the fit of the parameterizations?
- (iii) How do the three different tensor terms behave in deformed nuclei depending on the symmetries chosen for the nuclear shapes? For spherically symmetric systems, two of them reduce to the same functional form, whereas the third one vanishes.

The answers to these questions will to a large extent remain independent of remaining deficiencies of the central and spin-orbit interactions, and will be of great value for the construction of future improved energy functionals.

We will address the question of how the surface and surface symmetry energy coefficients change in dependence of the coupling constants of the tensor terms, and how this influences the deformation energy at large deformation in a future work.

## II. THE SKYRME ENERGY FUNCTIONAL WITH TIME-REVERSAL SYMMETRY

The total energy of a nucleus can be modeled by an energy density functional [2, 13, 14, 15] which is the sum of five terms: the uncorrelated kinetic energy, a Skyrme potential energy functional that models the strong interaction in the particle-hole channel, a pairing energy functional, a Coulomb energy functional whose exchange term is treated using the Slater approximation and correction terms that approximately remove the excitation energy due to spurious motions caused by broken symmetries

$$\mathcal{E} = \mathcal{E}_{\text{kin}} + \mathcal{E}_{\text{Sk}} + \mathcal{E}_{\text{pairing}} + \mathcal{E}_{\text{Coulomb}} + \mathcal{E}_{\text{corr}}. \quad (1)$$

The Skyrme energy density functional is local and can be decomposed into isoscalar  $t = 0$  and isovector  $t = 1$  contributions of central, spin-orbit and tensor terms

$$\mathcal{E}_{\text{Sk}} = \int d^3r \sum_{t=0,1} \mathcal{H}_t^{\text{Sk}}(\mathbf{r}) \quad (2a)$$

$$= \int d^3r \sum_{t=0,1} [\mathcal{H}_t^c(\mathbf{r}) + \mathcal{H}_t^{\text{ls}}(\mathbf{r}) + \mathcal{H}_t^t(\mathbf{r})]. \quad (2b)$$

The physics contained in the Skyrme functional has been discussed in great detail in the literature [2, 6, 15, 16, 17, 18]. We will repeat here only those aspects that are relevant for the present study.

### A. Local densities and currents

Each of the terms in the Skyrme energy density functional (2a) can be further decomposed into one part that depends on time-even densities only and another part that is bilinear in time-odd densities and currents [6, 15]. We follow the common practice to call them "time-even" and "time-odd" parts of the energy density functional, respectively, although the energy density functional  $\mathcal{E}$  itself is time-even by construction. Throughout this article, we will assume that time-reversal symmetry is not broken; hence, the densities and currents entering the time-odd part of the energy density functional vanish exactly. This allows one to represent the Skyrme part of the energy density functional through six independent local densities:

$$\rho_q(\mathbf{r}) = \rho_q(\mathbf{r}, \mathbf{r}')|_{\mathbf{r}=\mathbf{r}'}, \quad (3a)$$

$$\tau_q(\mathbf{r}) = \nabla \cdot \nabla' \rho_q(\mathbf{r}, \mathbf{r}')|_{\mathbf{r}=\mathbf{r}'}, \quad (3b)$$

$$J_{q,\mu\nu}(\mathbf{r}) = -\frac{i}{2}(\nabla_\mu - \nabla'_\mu) s_{q,\nu}(\mathbf{r}, \mathbf{r}')|_{\mathbf{r}=\mathbf{r}'} \quad (3c)$$

which are the scalar density  $\rho_q(\mathbf{r})$ , the scalar kinetic density  $\tau_q(\mathbf{r})$ , and the spin-current pseudotensor density  $J_{q,\mu\nu}(\mathbf{r})$  for protons and neutrons  $q = p, n$ . They can be constructed from neutron and proton density matrices expressed in the position basis [15, 18]

$$\begin{aligned} \rho_q(\mathbf{r}\sigma, \mathbf{r}'\sigma') &= \langle \hat{a}_{\mathbf{r}'\sigma'}^\dagger \hat{a}_{\mathbf{r}\sigma} \rangle \\ &= \frac{1}{2} \rho_q(\mathbf{r}, \mathbf{r}') \delta_{\sigma\sigma'} + \frac{1}{2} \mathbf{s}_q(\mathbf{r}, \mathbf{r}') \cdot \langle \sigma' | \hat{\boldsymbol{\sigma}} | \sigma \rangle, \end{aligned} \quad (4)$$

where

$$\begin{aligned} \rho_q(\mathbf{r}, \mathbf{r}') &= \sum_\sigma \rho_q(\mathbf{r}\sigma, \mathbf{r}'\sigma), \\ \mathbf{s}_q(\mathbf{r}, \mathbf{r}') &= \sum_{\sigma\sigma'} \rho_q(\mathbf{r}\sigma, \mathbf{r}'\sigma') \langle \sigma' | \hat{\boldsymbol{\sigma}} | \sigma \rangle. \end{aligned} \quad (5)$$

Proton and neutron densities can be recoupled to isoscalar  $t = 0$  and isovector  $t = 1$  densities, for example  $\rho_0(\mathbf{r}) = \rho_n(\mathbf{r}) + \rho_p(\mathbf{r})$  and  $\rho_1(\mathbf{r}) = \rho_n(\mathbf{r}) - \rho_p(\mathbf{r})$ , and similarly for  $\tau_t(\mathbf{r})$  and  $J_{t,\mu\nu}(\mathbf{r})$ .

The cartesian spin-current pseudotensor density  $J_{\mu\nu}(\mathbf{r})$  can be separated into its pseudoscalar, anti-symmetric vector and symmetric and traceless symmetric pseudotensor parts,

$$J_{\mu\nu}(\mathbf{r}) = \frac{1}{3} \delta_{\mu\nu} J^{(0)}(\mathbf{r}) + \frac{1}{2} \sum_{\kappa=x}^z \epsilon_{\mu\nu\kappa} J_\kappa^{(1)}(\mathbf{r}) + J_{\mu\nu}^{(2)}(\mathbf{r}), \quad (6)$$

where  $\delta_{\mu\nu}$  is the Kronecker symbol and  $\epsilon_{\mu\nu\kappa}$  the Levi-Civita tensor. The cartesian components of the pseudoscalar, vector and traceless pseudotensor parts, expressed in terms of the cartesian pseudotensor density, are given by

$$\begin{aligned} J^{(0)}(\mathbf{r}) &= \sum_{\mu=x}^z J_{\mu\mu}(\mathbf{r}), \\ J_\kappa^{(1)}(\mathbf{r}) &= \sum_{\mu,\nu=x}^z \epsilon_{\kappa\mu\nu} J_{\mu\nu}(\mathbf{r}), \\ J_{\mu\nu}^{(2)}(\mathbf{r}) &= \frac{1}{2} [J_{\mu\nu}(\mathbf{r}) + J_{\nu\mu}(\mathbf{r})] - \frac{1}{3} \delta_{\mu\nu} \sum_{\kappa=x}^z J_{\kappa\kappa}(\mathbf{r}). \end{aligned} \quad (7)$$

The radial component of  $\mathbf{J} = \sum_\kappa J_\kappa^{(1)} \mathbf{e}_\kappa$  is the only non-zero contribution when spherical symmetry is imposed. The pseudoscalar  $J^{(0)}(\mathbf{r})$  term still vanishes when rotational symmetry is broken, but parity remains conserved.

## B. Skyrme's tensor force

The Skyrme energy functional representing the central, tensor, and spin-orbit interactions can be written in different ways. The most traditional one [16, 17] is to

consider the functional as generated by a zero-range two-body effective interaction including a density-dependent term. In his seminal articles [19, 20], Skyrme introduced two tensor interactions that have not been considered in standard parameterizations so far. An "even" tensor force with the coupling constant  $t_e$  mixes relative  $S$  and  $D$  waves, whereas an "odd" tensor force with the coupling constant  $t_o$  mixes relative  $P$  and  $F$  waves

$$\begin{aligned} v^t(\mathbf{r}) &= \frac{1}{2} t_e \left\{ [3(\boldsymbol{\sigma}_1 \cdot \mathbf{k}')(\boldsymbol{\sigma}_2 \cdot \mathbf{k}') - (\boldsymbol{\sigma}_1 \cdot \boldsymbol{\sigma}_2) \mathbf{k}'^2] \delta(\mathbf{r}) \right. \\ &\quad \left. + \delta(\mathbf{r}) [3(\boldsymbol{\sigma}_1 \cdot \mathbf{k})(\boldsymbol{\sigma}_2 \cdot \mathbf{k}) - (\boldsymbol{\sigma}_1 \cdot \boldsymbol{\sigma}_2) \mathbf{k}^2] \right\} \\ &\quad + t_o \left[ 3(\boldsymbol{\sigma}_1 \cdot \mathbf{k}') \delta(\mathbf{r})(\boldsymbol{\sigma}_2 \cdot \mathbf{k}) - (\boldsymbol{\sigma}_1 \cdot \boldsymbol{\sigma}_2) \mathbf{k}' \cdot \delta(\mathbf{r}) \mathbf{k} \right], \end{aligned} \quad (8)$$

where we use the shorthand notation  $\mathbf{r} = \mathbf{r}_1 - \mathbf{r}_2$  for the relative position vector between the two particles, whereas  $\mathbf{k} = -\frac{i}{2}(\nabla_1 - \nabla_2)$  is the operator for relative momenta acting to the right and  $\mathbf{k}'$  its complex conjugate acting to the left. The vectors formed by the Pauli spin matrices are denoted by  $\boldsymbol{\sigma}_1$  and  $\boldsymbol{\sigma}_2$ .

With the symmetry restrictions that we have imposed, only the time-even part of the energy density corresponding to the tensor force (8) is different from zero and is given by

$$\begin{aligned} \mathcal{H}_t^t(v^t) &= -B_t^T \sum_{\mu,\nu=x}^z J_{t,\mu\nu} J_{t,\mu\nu} \\ &\quad - B_t^F \left[ \frac{1}{2} \left( \sum_{\mu=x}^z J_{t,\mu\mu} \right)^2 + \frac{1}{2} \sum_{\mu,\nu=x}^z J_{t,\mu\nu} J_{t,\nu\mu} \right] \end{aligned} \quad (9)$$

The labels of the coupling constants  $B_t^T$  and  $B_t^F$  refer to the time-odd terms they multiply in the energy functional when time-reversal invariance is broken, ensuring Galilean invariance [6]. The notation  $\mathcal{H}_t^t(v^t)$  stresses that Eq. (9) provides the contribution to tensor *terms* coming from the Skyrme zero-range tensor effective *interaction*  $v^t$  given by Eq. (8). When starting from the tensor force (8), the four coefficients  $B_t^T$  and  $B_t^F$  in Eq. (9) are determined by  $t_e$  and  $t_o$ . As discussed in the next section, the central part of Skyrme's interaction also gives rise to terms proportional to  $J_{t,\mu\nu} J_{t,\mu\nu}$  in the energy density [6, 15].

The three terms present in Eq. (9) couple the derivatives of the single-particle wave functions and the spin matrices in different ways. In the first term, the derivatives contained in both  $J_{t,\mu\nu}$  are taken along the same direction, as are the two Pauli spin matrices. The two other terms have a structure more typical of what is expected for a tensor interaction which couples a vector in space with a Pauli spin matrix. In the second term they are coupled within a given  $J_{t,\mu\mu}$ , whereas in the third term they are coupled between the  $J_{t,\mu\nu}$ s. It is the simultaneous presence of these three terms that is the signature of an actual tensor interaction.

### C. The Skyrme energy functional

The complete time-even part of the Skyrme energy density functional is obtained by combining the central, spin-orbit and tensor contributions

$$\begin{aligned} \mathcal{H}_t^{\text{Sk}} = & C_t^p[\rho_0] \rho_t^2 + C_t^{\Delta\rho} \rho_t \Delta\rho_t + C_t^\tau \rho_t \tau_t + C_t^{\nabla \cdot J} \rho_t \nabla \cdot \mathbf{J}_t \\ & - C_t^T \sum_{\mu, \nu=x}^z J_{t, \mu\nu} J_{t, \mu\nu} \\ & - C_t^F \left[ \frac{1}{2} \left( \sum_{\mu=x}^z J_{t, \mu\mu} \right)^2 + \frac{1}{2} \sum_{\mu, \nu=x}^z J_{t, \mu\nu} J_{t, \nu\mu} \right]. \end{aligned} \quad (10)$$

When the energy functional (10) is generated from a Skyrme interaction, the coupling constants  $C_t$  are the sum of the coupling constants  $A_t$  coming from the central and spin-orbit forces and those of the tensor force  $B_t$  and are defined in the appendix A of Article I.<sup>1</sup>

One can alternatively consider  $\mathcal{H}_t^{\text{Sk}}$  as a functional of local densities in a more general sense and abandon the link to effective interactions. The coefficients  $C_t$  are then fixed independently, except for constraints that must be imposed to fulfill Galilean invariance, cf. Article I. In principle, the twelve constants  $C_t$  can furthermore depend on densities, but in all standard Skyrme parameterizations extensively tested up to now, only  $C_t^p$  does depend on the isoscalar local density  $\rho_0$ .

### D. Choice of independent coupling constants in the energy density functional

The tensor terms are given in Eq. (10) as a function of the cartesian representation of the spin-current tensor density. Using the pseudoscalar, vector, and pseudotensor components  $J^{(0)}$ ,  $J^{(1)}$ , and  $J^{(2)}$  introduced in Eq. (7), which is more appropriate when spherical symmetry is imposed, one obtains an alternative form

$$\begin{aligned} \mathcal{H}_t^t = & -C_t^T \sum_{\mu, \nu=x}^z J_{t, \mu\nu} J_{t, \mu\nu} \\ & - C_t^F \left[ \frac{1}{2} \left( \sum_{\mu=x}^z J_{t, \mu\mu} \right)^2 + \frac{1}{2} \sum_{\mu, \nu=x}^z J_{t, \mu\nu} J_{t, \nu\mu} \right] \\ = & C_t^{J0} (J_t^{(0)})^2 + C_t^{J1} \mathbf{J}_t^2 + C_t^{J2} \sum_{\mu, \nu=x}^z J_{t, \mu\nu}^{(2)} J_{t, \mu\nu}^{(2)}. \end{aligned} \quad (11)$$

In the last line of Eq. (11) we have introduced new coupling constants for the terms bilinear in the pseudoscalar,

vector and pseudotensor parts of the spin-current pseudotensor density. Their relation to the coupling constants defined in Eq. (10) is given by

$$C_t^{J0} = -\frac{1}{3} C_t^T + \frac{2}{3} C_t^F, \quad (12a)$$

$$C_t^{J1} = -\frac{1}{2} C_t^T + \frac{1}{4} C_t^F, \quad (12b)$$

$$C_t^{J2} = -C_t^T - \frac{1}{2} C_t^F. \quad (12c)$$

In general, the tensor part of the energy density (10) depends on four independent parameters. This is most obvious in a cartesian representation of the tensor functional, where these four parameters are provided by the  $C_t^T$  and  $C_t^F$ . In Article I, however, we have used two different coupling constants to characterize the tensor terms that fulfill

$$C_0^J = 2 C_0^{J1}, \quad (13a)$$

$$C_1^J = 2 C_1^{J1}. \quad (13b)$$

These two coupling constants are sufficient to describe the strength of the isoscalar and isovector tensor terms in static<sup>2</sup> calculations in spherical symmetry as the pseudoscalar and pseudotensor parts of the spin-current tensor density are zero by construction.

When starting from a central and a tensor force, the ratios between the isospin components of the different terms will not be proportional, i.e.  $C_0^{J1}/C_1^{J1}$ ,  $C_0^{J2}/C_1^{J2}$ ,  $C_0^T/C_1^T$  and  $C_0^F/C_1^F$  will not be equal. The same property is lost also when one separates the tensor interaction strength between particles of the same and different isospins.

The tensor terms of existing Skyrme parameterizations have been adjusted on spherical nuclei, for which one has time-reversal invariance and  $\mathbf{J}_t^2$  is the only non-zero term in Eq. (11). Hence, the values of  $C_t^{J0}$  and  $C_t^{J2}$  have not been fixed by these fits and one has to make additional choices when going beyond sphericity. In the present work, parity is still conserved as a good quantum number such that the only problem is to fix the values of the two constants  $C_t^{J2}$ . The solution to this problem is not unique and a set of reasonable choices is given by:

- (i) One can consider that the tensor terms of the energy functional are generated by the central and tensor parts of a Skyrme force. There is then an univocal relation between  $C_t^{J2}$  and  $t_e$  and  $t_o$  and the balance between the various terms in Eq. (11) is automatically fixed. Unless otherwise noted, we will use this choice throughout the present article for the parameter sets *TIJ* introduced in Article I. This choice does not permit to set  $C_t^{J1}$  and  $C_t^{J2}$

<sup>1</sup> In the expressions of  $B_0^T$ ,  $B_1^F$ ,  $B_1^{\Delta s}$  and  $B_1^{\nabla s}$ , Eqns. (A3)-(A6) of the published version of Article I a global sign is missing, whereas the expressions given in the preprint are correct.

<sup>2</sup> We recall that in QRPA and other dynamical methods all components of  $J_{\mu\nu}$  might be non-zero in the response transition densities also in spherical symmetry, as do the time-odd densities not addressed here.

simultaneously to zero without imposing unrealistic constraints on the central Skyrme interaction. In particular, the parameterization T22 has been constructed in such a way that  $C_t^{J1} = 0$  and that the tensor terms vanish for spherical shapes. The values of  $C_t^{J2}$  are then non-zero and the contribution of the pseudotensor terms does not vanish for deformed shapes.

- (ii) Many authors set to zero the pseudotensor part of the tensor terms (11) for axially deformed Skyrme EDF calculations [21, 22] although it is *a priori* non-zero. They keep only the vector part  $\mathbf{J}$  that also appears in the spin-orbit part of the EDF. The main motivation for this choice is that the spin-current tensor density in cylindrical coordinates has a complicated form [23]. This can either be viewed as an approximation or as specific choice of the tensor terms such that  $C_t^{J2} = 0$ .
- (iii) Another possible choice is to set  $C_t^F$  to zero. Together with suitable choices for the time-odd part of the EDF, this allows to keep the functional form of the standard central Skyrme EDF, but with coupling constants of the symmetric tensor terms that are independent of those of a central Skyrme interaction. This choice has been made by the authors of Ref. [8].
- (iv) A choice similar to the previous one is to take  $C_t^T$  equal to zero, keeping only the antisymmetric combination of the spin-current tensor density.
- (v) Finally, one can take any ratio of  $C_t^F/C_t^T$  leading to a given  $C_t^{J1}$  value, which interpolates between the two previous choices.

When choosing  $C_t^{J1}$  and  $C_t^{J2}$  to be independent, we have the following interrelations between coupling constants

$$C_t^{J0} = -C_t^{J1} + \frac{5}{6}C_t^{J2}, \quad (14a)$$

$$C_t^T = -C_t^{J1} - \frac{1}{2}C_t^{J2}, \quad (14b)$$

$$C_t^F = 2C_t^{J1} - C_t^{J2}. \quad (14c)$$

The multitude of possible choices for the tensor parametrization opens the risk of an inconsistent use of the coupling constants of the tensor part of a given Skyrme parameterization. In particular, each choice leads to very different coupling constants in the "time-odd" part of the EDF, which can lead to significant differences.

Eventually, the bilinear part of the functional can be recoupled into terms that contain only densities of the same isospin on the one hand and terms that couple proton and neutron densities on the other hand. Such a representation is often used to characterize the interaction strength in the vector part of the tensor terms through coupling constants  $\alpha$  of the like-particle  $\mathbf{J}_t^2$  terms and  $\beta$  of the proton-neutron  $\mathbf{J}_t^2$  term

$$\alpha = C_0^J + C_1^J = 2(C_0^{J1} + C_1^{J1}), \quad (15a)$$

$$\beta = C_0^J - C_1^J = 2(C_0^{J1} - C_1^{J1}). \quad (15b)$$

The relation of  $\alpha$  and  $\beta$  to the coupling constants of Skyrme's central and tensor forces can be found in Article I. All other coupling constants of the energy density (10) can be recoupled in the same manner, of course.

### E. The single-particle Hamiltonian

The isospin representation of the EDF is very convenient for a discussion of its physical content. The codes that we have developed, however, use a different representation [17] that is better suited to construct the mean-fields with the symmetries chosen here. The central and spin-orbit parts of the Skyrme EDF have been described in Ref. [17]. The additional tensor terms that were not addressed are given by

$$\begin{aligned} \mathcal{H}^t = & b_{14} \sum_{\mu, \nu=x}^z J_{0, \mu\nu} J_{0, \mu\nu} \\ & + b_{16} \left[ \left( \sum_{\mu=x}^z J_{0, \mu\mu} \right)^2 + \sum_{\mu, \nu=x}^z J_{0, \mu\nu} J_{0, \nu\mu} \right] \\ & + \sum_{q=n,p} \left\{ b_{15} \sum_{\mu, \nu=x}^z J_{q, \mu\nu} J_{q, \mu\nu} \right. \\ & \left. + b_{17} \left[ \left( \sum_{\mu=x}^z J_{q, \mu\mu} \right)^2 + \sum_{\mu, \nu=x}^z J_{q, \mu\nu} J_{q, \nu\mu} \right] \right\}. \quad (16) \end{aligned}$$

The coupling constants of (16) are related to those of (11) through

$$\begin{aligned} b_{14} &= -C_0^T + C_1^T = C_0^{J1} - C_1^{J1} + \frac{1}{2}C_0^{J2} - \frac{1}{2}C_1^{J2} \\ b_{15} &= -2C_1^T = 2C_1^{J1} + C_1^{J2} \\ b_{16} &= -\frac{1}{2}C_0^F + \frac{1}{2}C_1^F = -C_0^{J1} + C_1^{J1} + \frac{1}{2}C_0^{J2} - \frac{1}{2}C_1^{J2} \\ b_{17} &= -C_1^F = -2C_1^{J1} + C_1^{J2}. \quad (17) \end{aligned}$$

The mean-field equations for protons and neutrons, obtained by functional derivative techniques [2, 15] from the energy functional (16), read

$$\hat{h}_q(\mathbf{r}) \psi_i(\mathbf{r}) = \epsilon_i \psi_i(\mathbf{r}), \quad (18)$$

with the one-body Hamiltonian corresponding to the energy functional (10) given by<sup>3</sup>

$$\hat{h}_q(\mathbf{r}) = U_q(\mathbf{r}) - \nabla \cdot B_q(\mathbf{r}) \nabla$$

---

<sup>3</sup> For the standard Skyrme functional (11) with non-density-dependent coupling constants of the spin-orbit and tensor terms, the second line can be simplified into  $-i \sum_{\mu\nu} W_{q, \mu\nu}(\mathbf{r}) \nabla_\mu \hat{\sigma}_\nu$  for the symmetries chosen here.



$$-\frac{i}{2} \sum_{\mu, \nu=x}^z [W_{q, \mu \nu}(\mathbf{r}) \nabla_{\mu} + \nabla_{\mu} W_{q, \mu \nu}(\mathbf{r})] \hat{\sigma}_i (19)$$

where the  $\hat{\sigma}_{\nu}$  denote the Pauli matrices. The expressions for the single-particle potential  $U(\mathbf{r})$  and the inverse effective mass  $B(\mathbf{r})$  are the same as those given in Ref. [17]. When the energy functional depends on the vector part of the spin-current tensor only, the second line of Eq. (19) boils down to  $-i \mathbf{W}_q(\mathbf{r}) \cdot \nabla \times \boldsymbol{\sigma}$  with  $\mathbf{W}_q(\mathbf{r}) = \sum_{\mu \nu \kappa} \epsilon_{\mu \nu \kappa} W_{q, \mu \nu}(\mathbf{r}) \mathbf{e}_{\kappa}$ , where  $\mathbf{e}_{\kappa}$  is the unit vector in  $\kappa$  direction. With the full spin-current tensor, one has to consider

$$\begin{aligned} W_{q, \mu \nu}(\mathbf{r}) &= \frac{\delta E}{\delta J_{q, \mu \nu}(\mathbf{r})} \\ &= -b_9 \sum_{\kappa=x}^z \epsilon_{\kappa \mu \nu} (\nabla_{\kappa} \rho + \nabla_{\kappa} \rho_q) \\ &\quad + 2b_{14} J_{\mu \nu} + 2b_{15} J_{q, \mu \nu} + 2b_{16} J_{\nu \mu} + 2b_{17} J_{q, \nu \mu} \\ &\quad + 2b_{16} \left[ \sum_{\kappa=x}^z J_{\kappa \kappa} \right] \delta_{\mu \nu} + 2b_{17} \left[ \sum_{\kappa=x}^z J_{q, \kappa \kappa} \right] \delta_{\mu \nu} \quad (20) \end{aligned}$$

instead. The terms in the first line of Eq. (20) originate from the spin-orbit part of the functional, the other two lines from the tensor part. The terms in the last line of Eq. (20) might be nonzero only when parity is broken.

We recall that for constrained calculations, as discussed below, the constraints do not contribute to the observable total energy, which is still obtained from  $\mathcal{E}$ , Eq. (1), whereas the eigenvalues  $\epsilon_i$  of the mean-field Hamiltonian used to construct the Nilsson diagrams contain a contribution from the constraint [24].

### III. PARAMETERIZATIONS

For an overview of earlier choices made for the coupling constants of the tensor terms in standard parameterizations of the Skyrme energy functional, we refer to Article I. We will limit ourselves here to recent parameterizations that explore the impact of tensor terms on single-particle spectra.

#### A. $TIJ$ parameterizations of Lesinski *et al*

The main aim of the present article is to test the deformation properties of magic and semi-magic nuclei obtained with the parameterizations  $TIJ$  introduced in Article I. The fit of these parameterizations is based on the same protocol as the one of the  $SLy x$  parameterizations [13, 14], with a few minor changes explained in Article I. We have found in Article I that to add a tensor term to a standard Skyrme EDF does not globally correct its deficiencies for the prediction of masses, radii, or

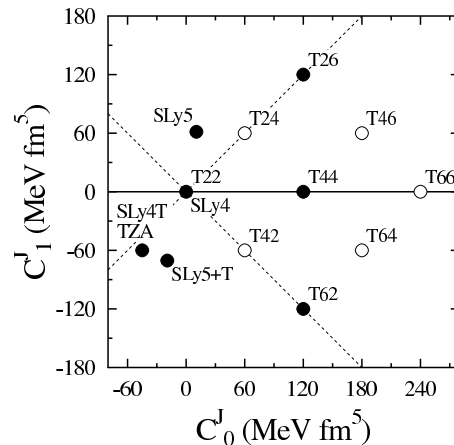


FIG. 1: Coupling constants  $C_0^J$  and  $C_1^J$  of the tensor terms for the parameterizations discussed in the paper.

single-particle properties of semi-magic nuclei. In fact, very different values of the  $C_t^J$  constants are required for each of these observables to be accurately reproduced, and even these values should vary in different mass regions. Instead of trying to construct a single "best" EDF in Article I, we have studied the impact of the tensor terms on different observables by constructing a set of 36 parameterizations, each corresponding to given values of  $C_0^J$  and  $C_1^J$ , and all other Skyrme parameters being determined by the same fitting procedure. In this way, a wide range of the effective coupling constants  $C_0^J$  and  $C_1^J$  is systematically covered.

In the present study, we limit ourselves to a small subset of these 36 parameterizations, i.e. T22, T26, T44, and T62 in most cases. Figure 1 shows their location in the parameter space of  $C_0^J$  and  $C_1^J$ . The parameterization T22 has by construction vanishing tensor terms at sphericity. It should have properties close to those of SLy4 in which tensor terms have been neglected. The parameterizations T26, T44 and T62 share the same value of the isoscalar tensor coupling constant  $C_0^J = 120 \text{ MeV fm}^5$ , and differ by the isovector one  $C_1^J$ , which takes the values 120, 0 and  $-120 \text{ MeV fm}^5$  respectively.

Parameterizations having the same proton-neutron coupling constant  $\beta$  are aligned along the first diagonal in Fig. 1, those with the same value of  $\alpha$  are aligned along the anti-diagonal. For parameterizations  $TIJ$ , the coefficient of the proton-neutron tensor term increases with the first index  $I$  for the fixed like-particle tensor term, whereas that of the like-particle tensor term increases with the second index  $J$  for fixed proton-neutron tensor coupling. Let us recall that the integers  $I$  and  $J$  are related to the constants  $\alpha$  and  $\beta$  by

$$\alpha = 60(J - 2) \text{ MeV fm}^5, \quad (21a)$$

$$\beta = 60(I - 2) \text{ MeV fm}^5. \quad (21b)$$

TABLE I: Skyrme parameterizations discussed in this work. Procedure: Variational (V) corresponds to Skyrme parameterizations where, for given tensor coefficients, all other Skyrme parameters are fitted following the procedure of Ref. [14], slightly modified in Article I for the  $TIJ$  interactions, while perturbative (P) labels parameterizations for which tensor terms are added without refit. Type: the parameterization is treated as an interaction (I) or a functional (F). Central: the contribution to the tensor terms coming from the central part of the interaction is included or not. Tensor: a tensor interaction is included or not

	procedure	type	central	tensor	Ref.	remarks
SLy4	V	I	N	N	[14]	The tensor contributions from the central part of the interaction are neglected.
SLy5	V	I	Y	N	[14]	
$TIJ$	V	I	Y	Y	[6]	Isovector tensor coefficients equal to zero if $I = J$
T22	V	I	Y	Y	[6]	Central and tensor contributions to the tensor terms such that they cancel each other at sphericity (close to SLy4)
SLy4T	P	F	-	-	[8]	Refit of SLy4T on masses keeping tensor and spin-orbit coefficients fixed
SLy4T <sub>min</sub>	V	F	-	-	[8]	
SLy5+T	P	I	Y	Y	[5]	
SLy4T <sub>self</sub>	V	I	Y	Y	this work	Refit of SLy4T with the same protocol as $TIJ$ keeping the same spin-orbit and tensor coefficients for spherical shapes as in Ref. [8]
TZA	V	I	Y	Y	this work	Refit of SLy4T with the same protocol as $TIJ$ for the tensor coefficients used in Ref. [8]

### B. The parameterization of Colò *et al.*

The Skyrme parameterization SLy5 introduced in Ref. [14] is one of the two SLy $x$  functionals which include the tensor terms generated from the central part of the Skyrme force. Colò *et al.* [5] have added a tensor force to it, keeping all the other coupling constants of the parameterization at their original values. We will call this interaction SLy5+T ("SLy5 plus tensor") in what follows. The parameters of the tensor force were adjusted in spherical symmetry to single-particle energies along the chains of  $N = 82$  isotones and  $Z = 50$  isotopes. The empirical values for these energies were obtained as separation energies of the last particle in states of an odd- $A$  nucleus, assumed to be dominated by one single-particle configuration. They were compared to the eigenvalues of the one-body Hamiltonian, Eq. (19), in the neighboring even-even nucleus. The resulting coupling constants in MeV fm<sup>5</sup> are  $C_0^J = -19.333$  and  $C_1^J = -70.466$ , or, equivalently,  $\alpha = -89.8$  and  $\beta = 51.9$ . This parameterization has been used in studies of spherical shell structure in Ref. [7] and of the Gamov-Teller strength distribution in <sup>90</sup>Zr and <sup>208</sup>Pb through RPA calculations in Ref. [25, 26]. As can be seen in Fig. 1, SLy5+T explores a different region of the parameter space than the  $TIJ$  parameterizations;  $\alpha$  being negative and its modulus larger than  $\beta$ .

### C. The parameterization of Zalewski *et al.*

In Ref. [8], Zalewski *et al.* did refit the spin-orbit and tensor coupling constants of some standard Skyrme interactions. We will consider here two of their fits that are based on the SLy4 functional [14]. In a first step, Zalewski *et al.* readjusted  $C_t^{\nabla J}$  and  $C_t^J$  to carefully selected spin-orbit splittings in <sup>40</sup>Ca, <sup>48</sup>Ca and <sup>56</sup>Ni, keeping all other coupling constants of the energy functional at their original values. The single-particle energies of a spherical mean-field calculation of doubly-magic nuclei have been identified with the separation energy of a nucleon with the same quantum numbers to or from the odd neighboring nuclei. They were compared to experimental separation energies corrected through a macroscopic model taking into account the influence of the coupling of the single-particle state to collective vibrations of the surface. The values of the parameters resulting from this procedure are  $C_0^J = -45$ ,  $C_1^J = -60$ ,  $C_0^{\nabla J} = -60$  and  $C_1^{\nabla J} = -20$  (all in MeV fm<sup>5</sup>) and define an EDF called SLy4T. The strength of the standard zero-range spin-orbit force of SLy4T is equal to  $W_0 = 80$  MeV fm<sup>5</sup> and is much lower than in the original SLy4 parameterization, for which  $W_0 = 123$  MeV fm<sup>5</sup>.

Such a modification of  $C_t^J$  and  $C_t^{\nabla J}$  from their original values without changing the other parameters of the EDF degrades prohibitively the masses calculated with SLy4T with respect to those obtained with SLy4. For this reason, Zalewski *et al.* refitted all parameters of SLy4T except  $C_t^J$  and  $C_t^{\nabla J}$  in a second step to restore a reasonable description of bulk properties, leading to the parameterization SLy4T<sub>min</sub>.

The parameterizations SLy4T and SLy4T<sub>min</sub> are explicitly constructed as energy density functionals without making reference to any underlying central, spin-orbit, or tensor force. In particular, the authors chose to set the two coupling constants  $C_t^F$  of the asymmetric cartesian tensor term to zero and to vary only  $C_t^T$ . This automatically fixes the value of  $C_t^{J2}$  to be equal to two times that of  $C_t^{J1}$  for  $t = 0$  and  $t = 1$ . Although the coupling constants  $C_t^{\nabla J}$  of the spin-orbit term were readjusted, the ratio between the isoscalar and isovector coupling constants  $C_0^{\nabla J}/C_1^{\nabla J}$  was kept at the value of the original fit.

To analyze the consequences of the choices made in the fitting strategy of Zalewski *et al.* and those of Article I, we performed two additional fits using the same protocol as in Ref. [6], but exploring a different region around  $(-45, -60)$  MeV fm<sup>5</sup> corresponding to SLy4T in the  $C_0^J, C_1^J$  plane of Fig. 1. For the first one, called SLy4T<sub>self</sub> hereafter, we fixed  $C_t^J$  and  $C_t^{\nabla J}$  at their SLy4T values, but readjusted all the other constants of the functional to obtain the "best" EDF corresponding to our protocol. This parameterization differs from SLy4T<sub>min</sub> by the fit protocol, and by our choice to keep the interrelations between the coupling constants of the tensor terms as obtained from a two-body central and tensor forces. To study also the impact of the readjustment of the spin-orbit interaction, we constructed a second parameterization, called TZA hereafter, where we additionally vary  $W_0$ , resulting to a value  $W_0 = 111.934$  MeV fm<sup>5</sup>. This parameterization is thus fitted exactly as the *TIJ* ones, except that it is outside of the rectangular parameter space for  $C_0^J$  and  $C_1^J$  considered in Article I. The coupling constants for SLy4T<sub>self</sub> and TZA can be found in the *Physical Review* archive [27]. The properties of all the interactions that we have used are summarized in Table I.

## IV. RESULTS

### A. Technical Details

The wave functions are constructed with the code EV8 [28, 29] which has been modified to include the tensor terms in the energy density functional and the single-particle Hamiltonian. The energies have been recalculated after convergence with a code that uses a more accurate algorithm for the derivatives.

Pairing correlations are treated with the Lipkin-Nogami (LN) method to avoid the breakdown of BCS pairing and the resulting discontinuities in the deformation energy curves. We use an effective density-dependent zero-range pairing interaction with two soft cutoffs at 5 MeV above and below the Fermi energy as described in Ref. [30]. For consistency with our recent calculations [31, 32], we chose a strength of  $-1000$  MeV fm<sup>-3</sup> for light and medium-heavy nuclei and  $-1250$  MeV fm<sup>-3</sup> for <sup>186</sup>Pb and <sup>208</sup>Pb.

### B. General comments

The magic numbers close to stability can be divided into two categories: up to 20, they correspond to a spin-saturated closure of major oscillator shells, whereas above 20, they are created by the spin-orbit interaction which pushes down the level with largest  $j$ -value into the gap between the oscillator shells for 28, or even into the oscillator shell below the gap for 50, 82 and 126. One usually labels a spherical nucleus spin saturated when all pairs of spin-orbit partners are either occupied or empty. In realistic mean-field calculations this will not result in an exact cancellation of the spin-current tensor density, as it should be the case for an exact spin saturation. This has two origins. First, the radial wave functions of the spin-orbit partners are not identical, and, second, pairing correlations will smear out the distribution of occupation numbers. The effect of these two factors will be discussed in a forthcoming publication [33]. Tensor terms in the time-even part of the energy functional fluctuate with the spin-current tensor density  $J_{\mu\nu}$ , which is small in spin-saturated systems, and large whenever only the lower level of a pair of spin-orbit partners is filled, while its partner level remains empty. For an illustration we refer to Article I.

Deformation breaks this simple picture. As soon as it sets in, the spin saturation or non-saturation disappears and the energy due to tensor terms varies in a way related to the sign of the coupling constants. Close to sphericity, this can be determined by looking at the  $C_t^J$  coefficients. For  $N = Z$  spin saturated nuclei and parameterizations with  $C_0^J$  positive, the contribution from the tensor interaction is zero at sphericity and becomes repulsive as soon as deformation sets in. For  $N = Z$  spin-unsaturated nuclei, the tensor contribution will be largest at sphericity and decrease with deformation.

### C. <sup>56</sup>Ni

Let us start our study by looking in detail into <sup>56</sup>Ni, the lightest doubly-magic nucleus with major proton and neutron shell closures due to the spin-orbit interaction. The values and systematics of static [34] and transition moments [35] of low-lying states around <sup>56</sup>Ni suggest that it is not as good an inert magic core as other doubly-magic nuclei. This feature is also observed in shell-model calculations [36] and is at the origin of substantial corrections found between "empirical" and "bare" single-particle energies in Ref. [37]. Several well-deformed rotational bands coexisting with the spherical shell-model-type states have been observed, one of them down to a 2<sup>+</sup> level at 5.351 MeV [38].



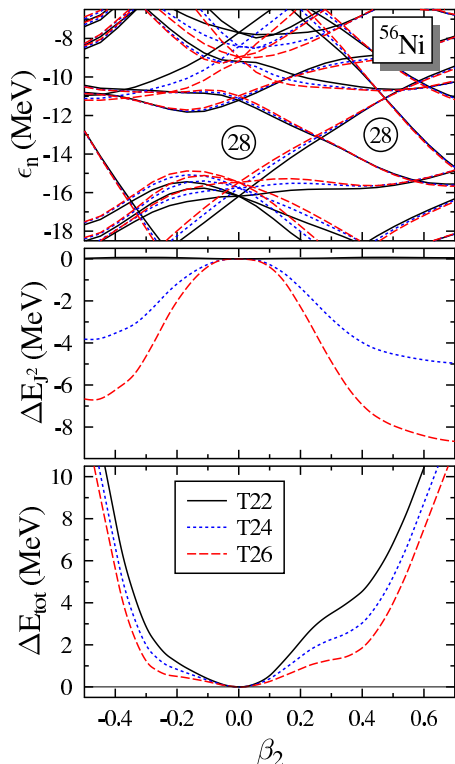


FIG. 2: (Color online) Nilsson diagram of the neutrons (top), change of the total contribution from the tensor terms to the total energy relative to the values at the spherical shape (middle) and deformation energy relative to the spherical shape (bottom) for  $^{56}\text{Ni}$  obtained with the parameterizations T22, T24 and T26. The energy scale is the same for the two lower panels.

### 1. Key quantities

Figure 2 provides three key quantities for the analysis of the deformation properties of  $^{56}\text{Ni}$ : the neutron Nilsson diagram, the contribution of tensor terms to the deformation energy and the total energy, all as a function of axial quadrupole deformation. Three parameterizations have been used, T22, T24 and T26, which differ in the strength of the tensor terms. The proton Nilsson diagram is very similar to the one for neutrons, except for an overall shift due to the Coulomb interaction. The dependence of these quantities on the axial quadrupole deformation is shown as a function of the dimensionless deformation  $\beta_2$  of the mass density distribution defined as

$$\beta_2 = \sqrt{\frac{5}{16\pi}} \frac{4\pi}{3R^2A} \langle 2z^2 - y^2 - x^2 \rangle, \quad (22)$$

where  $R = 1.2 A^{1/3}$  fm.

The presence of tensor terms in the energy functional has an obvious impact on the single-particle levels. An increase of the tensor interaction results in a reduction of the spin-orbit fields and in a smaller spherical gap at  $N = 28$ . The net result is a sizable decrease of the splitting

of the  $1f$  levels from T22 to T62. At the same time, tensor terms also modify the slope of the Nilsson levels at small deformations, whereas, at large deformation, the levels predicted by the three parameterizations nearly lie on top of each other.

At sphericity, the tensor contribution for T22 is zero by construction. In practice, one can see that the tensor energy remains close to zero for all deformations. As soon as the nucleus is deformed, the decrease of spin non-saturation strongly affects the tensor terms. Parameterizations like T24 and T26 have a positive like-particle coupling constant  $\alpha$  and give repulsive tensor energies at sphericity. This repulsion is decreased by deformation, which reduces the tensor terms by several MeV. For T26, the total energy curve obtained as a function of deformation is softer than without the tensor interaction. In particular, the shoulder at prolate deformations becomes lower in energy and more pronounced. This structure is associated with the rotational band observed down to spin  $2^+$  [38]. The gain in total deformation energy, however, is much smaller than the gain in deformation energy from the tensor terms.

In the following subsections, we will analyze the origin of these differences and their dependence on the fit strategy.

### 2. Contributions to the total energy

Let us first recall that the interactions constructed in Article I differ not only by their choice of the strengths of the tensor interaction, but that all the other terms of the energy functional are also different because each interaction is refitted on the same set of data. It is, therefore, interesting to examine how the different terms of the functional vary from one set to another and how the changes induced by the tensor interaction are, in fact, largely attenuated by a readjustment of the entire functional.

Figure 3 presents the decomposition of the total binding energy into the contributions from the various terms in the energy functional, Eq. (1), for parameterizations T22, T24 and T26. Those panels showing contributions to the Skyrme energy functional are labeled by their content in densities, Eq. (10), whereas the other panels provide the kinetic energy (plus the one-body center-of-mass correction), the Coulomb energy and the pairing energy (including the Lipkin-Nogami correction).

Unlike in Fig. 2, Fig. 3 shows here the absolute values for the total binding energy and the tensor contributions. The binding energy of  $^{56}\text{Ni}$  is included in the data the  $\text{TIJ}$  parameterizations are adjusted to and, indeed, the total energy (lower left panel) differs by only a few 100 keV at sphericity. Also, as already pointed out, the deformation energy curves obtained with the three parameterizations differ by less than 2 MeV. These similarities result from a complicated compensation between the various components of the energy. All of them, with

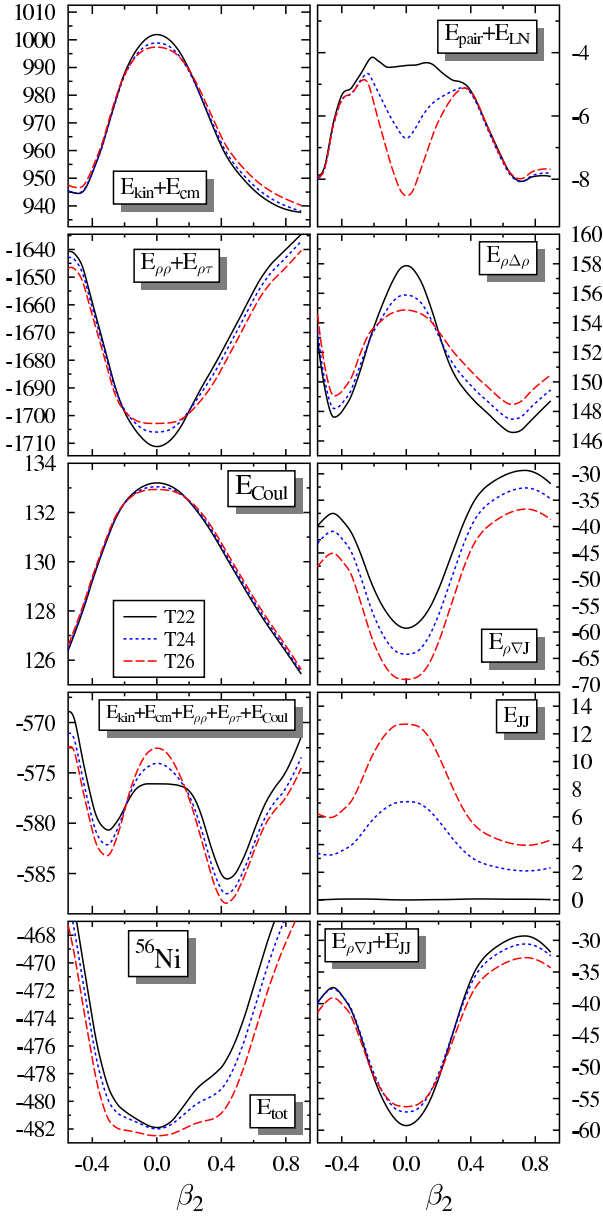


FIG. 3: (Color online) Decomposition of the total energy of  $^{56}\text{Ni}$  obtained with the parameterizations T22, T24 and T26 into the various contributions to the EDF, Eqns. (1) and (10), as a function of the quadrupole deformation  $\beta_2$  (see text).

the exception of the Coulomb energy, differ on a much larger scale, both in absolute values and deformation dependence.

It can be seen also that each term of the EDF has a very different dependence on deformation and that the total deformation energy also always results from subtle compensations. Both the kinetic energy and the part of the Skyrme functional that contributes to  $E/A$  in infinite homogeneous nuclear matter,  $C^\rho[\rho]\rho^2 + C^\tau\rho\tau$ , vary by about 70 MeV as a function of deformation. The part of the EDF that does not depend on gradient terms is obtained by summing these two terms and the Coulomb

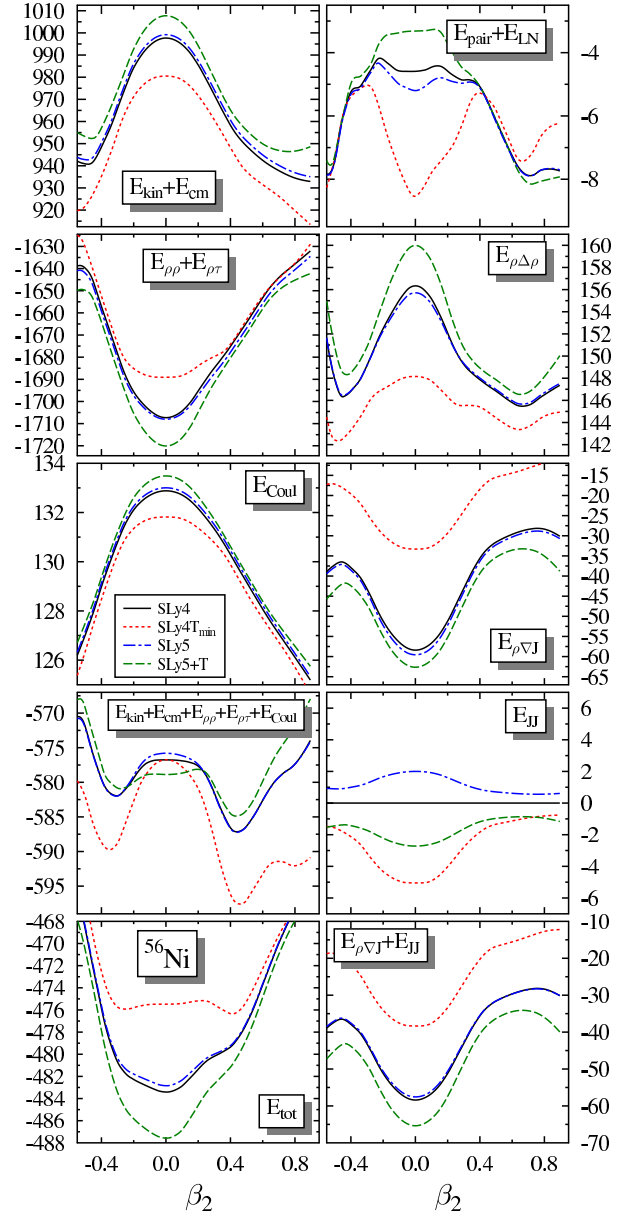


FIG. 4: (Color online) Same as Fig. 3, but for the parameterizations SLy4, SLy4T<sub>min</sub>, SLy5, and SLy5+T.

energy, and is represented in the panel in the fourth row on the left. It varies with deformation by about 15 MeV. For all parameterizations, the latter curves exhibit pronounced prolate and oblate minima. The gradient term  $C^{\Delta\rho}\rho\Delta\rho$  even amplifies the preference for deformed minima. The combined spin-orbit and tensor terms, shown individually and summed up in the three lower right panels, are the necessary ingredient to obtain a spherical ground state in  $^{56}\text{Ni}$ . This underlines the fact that the spin-orbit and tensor terms are not only important for single-particle spectra, but also might play a crucial role for the total binding energy, in particular for its deformation dependence. Interestingly, for this nucleus and the parameterizations shown, the contributions of the spin-

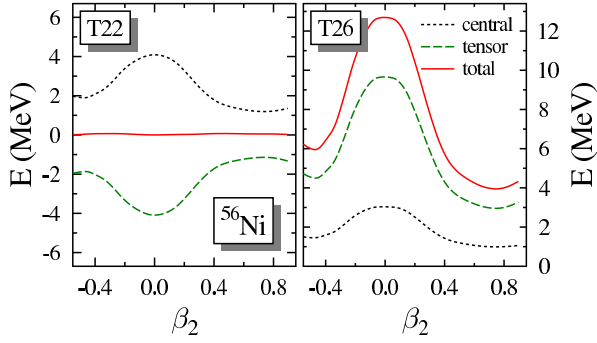


FIG. 5: (Color online) Decomposition of the isoscalar tensor energy obtained in  $^{56}\text{Ni}$  for the parameterizations T22 and T26 into the contributions from the central and tensor parts of the forces.

orbit and tensor terms are of opposite sign and sum up such that their sum is much less dependent on the parameterization than the individual terms.

Figure 4 provides the same decomposition for various variants of SLy4 adjusted with different strategies, i.e. SLy4, SLy5, SLy4T<sub>min</sub> and SLy5+T.

The results obtained with the two functionals SLy4 and SLy5 adjusted in Ref. [14] are quite close for all terms, except of course for the tensor contribution, excluded in the case of SLy4 and restricted to the contribution from the central interaction for SLy5. All components of the energy differ slightly since the coupling constants are completely refitted in both cases. The total energies obtained with these two parameterizations, however, are quite close.

In particular, although SLy4 and SLy5 correspond to slightly different coupling constants, they lead to results which differ on a much smaller scale than SLy5 and SLy5+T, which differ only by the tensor terms. This underlines the role of self-consistency: the difference in the tensor terms is responsible for changes in the single-particle properties, which ultimately induce changes in each individual contribution to the energy functional.

The similarity between the curves obtained with SLy4 and T22 (Fig. 3 and Fig. 4), shows that the slight differences between the interactions have no significant effect.

### 3. Decomposition of the tensor terms

The energy contribution from the tensor terms can be decomposed in several ways. We first compare the contributions from the central and tensor parts of the parameterizations T22 and T26 in Fig. 5. As explained in Sect. II D, such a decomposition has a meaning only when assuming an underlying force, but not for genuine functionals. The central contribution is very similar for both parameterizations (and all others from the  $TIJ$  family), which is a consequence of its correlation with effective masses and surface tensions through  $t_1$  and  $t_2$  terms of the two-body Skyrme force, see the discussion of Fig. 3 in

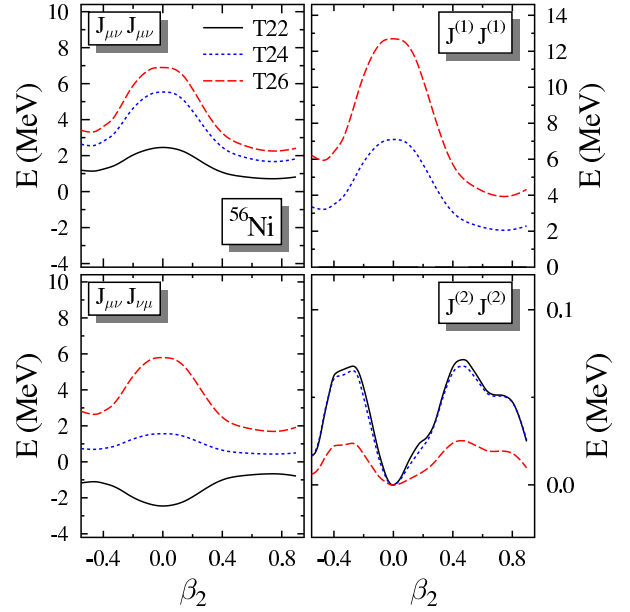


FIG. 6: (Color online) Decomposition of the isoscalar tensor energy obtained in  $^{56}\text{Ni}$  for the parameterizations T22, T24 and T26 into the contributions from symmetric and asymmetric terms in the cartesian representation (left), or the contributions from vector and pseudotensor contributions (right). The same energy scale is used for all panels except the one for the pseudotensor contribution  $J^{(2)} J^{(2)}$ .

Article I. The contribution from central and tensor parts cancel nearly exactly for T22 for all deformations. As exemplified by T26, the contributions from the central and tensor forces to the tensor terms have the same sign for  $^{56}\text{Ni}$  for all other  $TIJ$  parameterizations that have zero or positive values for  $C_0^J$  and  $C_1^J$ .

In Fig. 6, we decompose the tensor energy in the cartesian and in the angular-momentum coupled representations. Isovector contributions for this  $N = Z$  nucleus are smaller than 20 keV for all deformations. In the left panels, the contributions corresponding to the symmetric and asymmetric terms in the cartesian representation are plotted. Both are of the order of a few MeV for T22 and of opposite sign to ensure a total contribution close to zero. They are also of similar magnitude for T26, but repulsive in both cases. Results from T24 are intermediate between those of T22 and T26. The right panels show the contributions to the total tensor energy from the vector and pseudotensor terms in the angular-momentum coupled representation. The contribution from the pseudoscalar term is zero with the symmetries assumed here. Except for T22, where the vector contribution is zero by construction, the pseudotensor contribution is two orders of magnitude smaller than the vector one. We found similar results for all other parameterizations with nonzero  $C_0^{J1}$  and for all nuclei studied here. This justifies the common practice of neglecting the pseudotensor terms for the purpose of calculating binding energies in situations where Galilean invariance is not an issue.

TABLE II: Eigenvalues corresponding to the neutron  $pf$  and the  $g_{9/2+}$  orbitals obtained for the single-particle Hamiltonian at spherical shape in  $^{56}\text{Ni}$  (see text).

parameterization	$\epsilon_{f_{7/2}}$	$\epsilon_{f_{5/2}}$	$\Delta\epsilon_f$	$\epsilon_f^{\text{cent}}$	$\epsilon_{p_{3/2}}$	$\epsilon_{p_{1/2}}$	$\Delta\epsilon_p$	$\epsilon_p^{\text{cent}}$	$\Delta\epsilon_f/\Delta\epsilon_p$	$\epsilon_f^{\text{cent}} - \epsilon_p^{\text{cent}}$	$\epsilon_{g_{9/2}}$
experiment ( $\pm S_{1n}$ )	-16.64	-9.48	1.02	-13.57	-10.25	-9.14	0.37	-9.88	2.75	3.69	—
empirical [37]	-16.93	-9.53	1.06	-13.76	-10.36	-8.48	0.63	-9.73	1.68	4.03	—
T22	-16.18	-7.70	1.21	-12.54	-11.21	-9.19	0.67	-10.54	1.80	2.00	-4.26
T26	-15.47	-8.97	0.93	-12.68	-10.98	-9.19	0.60	-10.38	1.56	2.30	-3.56
T44	-15.56	-8.69	0.98	-12.61	-11.09	-9.20	0.63	-10.46	1.56	2.15	-3.75
T62	-15.61	-8.52	1.01	-12.57	-11.22	-9.25	0.66	-10.56	1.54	2.00	-3.89
SLy5	-16.01	-8.03	1.14	-12.59	-11.11	-9.17	0.65	-10.47	1.76	2.12	-4.05
SLy5+T	-16.66	-7.09	1.37	-12.56	-11.15	-9.01	0.72	-10.44	1.91	2.12	-4.67
SLy4	-16.17	-7.80	1.20	-12.58	-11.13	-9.14	0.66	-10.47	1.81	2.11	-4.20
SLy4T	-15.49	-8.71	0.97	-12.58	-11.20	-9.47	0.57	-10.62	1.69	1.96	-3.54
SLy4T <sub>min</sub>	-15.63	-8.72	0.99	-12.67	-11.26	-9.50	0.59	-10.67	1.68	1.98	-3.57
SLy4T <sub>self</sub>	-15.73	-8.59	1.02	-12.67	-11.29	-9.50	0.60	-10.70	1.70	1.97	-3.71
TZA	-16.57	-7.08	1.36	-12.50	-11.33	-9.18	0.72	-10.61	1.90	1.89	-4.65

All decompositions of the tensor energy exhibit the same trend: this energy decreases with deformation, without exhibiting much structure. This behavior can be understood rather easily in this  $N = Z$  nucleus where the  $f_{7/2-}$  orbitals are filled at sphericity while the  $f_{5/2-}$  ones are empty. This situation makes the tensor interaction maximal. As soon as deformation sets in, this simple picture is destroyed: the single-particle levels loose their purity and cross, cf. the upper panel of Fig. 2.

#### 4. Single-particle spectra at sphericity

We give in Table II the eigenvalues of the single-particle Hamiltonian  $\hat{h}_q$ , Eq. (18) for neutron orbitals in the  $pf$  shell obtained in calculations of  $^{56}\text{Ni}$  imposing spherical shape. The position of the  $1g_{9/2+}$  level is also given, although it is far above the Fermi energy at spherical shape, as it determines the size of the deformed gap at 28 in the Nilsson diagram through its downsloping  $j_z = 1/2$  levels, cf. Fig. 2.

We also give the renormalized spin-orbit splittings

$$\Delta\epsilon_\ell = \frac{1}{2\ell+1}(\epsilon_{j=\ell-1/2} - \epsilon_{j=\ell+1/2}), \quad (23)$$

which for a standard modified oscillator potential would be independent on the quantum numbers of the single-particle states, the centroids

$$\epsilon_\ell^{\text{cent}} = \frac{\ell+1}{2\ell+1}\epsilon_{j=\ell+1/2} + \frac{\ell}{2\ell+1}\epsilon_{j=\ell-1/2}, \quad (24)$$

of spin-orbit partners for the  $2p$  and  $1f$  levels, the ratio  $\Delta\epsilon_f/\Delta\epsilon_p$  of the spin-orbit splittings of the  $1f$  and  $2p$  levels, and the distance of their centroids  $\epsilon_f^{\text{cent}} - \epsilon_p^{\text{cent}}$ .

Experimental separation energies from or into low-lying levels in the odd- $A$  neighbors of  $^{56}\text{Ni}$  that have the characteristics of a single-particle configuration are given in the first line of Table II. Empirical values for the single-particle energies are given in the second line. These quantities are usually compared to the eigenvalues  $\epsilon_i$  of the mean-field hamiltonian, although many factors make this comparison questionable, see for instance [8] and Sect. IV. B of Article I. One source of ambiguity is the coupling of the particle or hole outside the closed shell to the vibrations of the core. Using the schematic extended unified model, the authors of [37] attempted to remove this effect to determine "bare" values of the single-particle energies by reverse engineering from the low-lying excitation spectra of  $^{56}\text{Ni}$  and its odd- $A$  neighbors. Although model-dependent, we include these values here in the second line of Table II to have a rough estimate of the order of magnitude of the corresponding corrections. In any event, for an  $N = Z$  nucleus such as  $^{56}\text{Ni}$ , there is also a contribution from the Wigner energy to the separation energies [39], which is not considered in Ref. [37]. Its main effect for a magic nucleus is to render the gap in the separation energies much larger than the gap in the spectrum of eigenvalues of the mean field. Using a schematic model, Chasman [39] estimates the correction from the Wigner energy to the size of the  $N = 28$  gap in the empirical spectrum from separation energies to be larger than 2 MeV.

The results for the parameterizations T22, T26, T44 and T62 are given in the next four lines. By construction, there is no tensor contribution at sphericity for T22. The other three interactions share the same isoscalar coupling constant  $C_0^J = 120 \text{ MeV fm}^5$ , but differ in their isovector one  $C_1^J$ . The presence of a tensor term has a small effect on the absolute position of the  $2p$  levels, which move

at most by 200 keV, much less than the  $1f$  levels for which the changes go up to 1.2 MeV. The tensor term is mainly responsible for a reduction of the spin-orbit splittings, whereas the centroids of the  $2p$  and  $1f$  levels are affected to a much smaller extent. A change in the centroid position cannot be directly related to the tensor terms since they do not contribute directly to the part of the mean field which governs it. The modification of the centroids is a non-linear effect induced by the tensor. Although small, the net effect is visible, in particular for the distance between the  $1f$  and  $2p$  centroids that are pulled into opposite directions.

The shift of the centroids is correlated to the isoscalar tensor coupling constants (cf. T22 and T44), but unexpectedly for a  $N = Z$  nucleus, also slightly to the isovector ones (cf. T26, T44 and T62). The isovector densities and currents induced by the isospin breaking Coulomb interaction are small and do not significantly contribute to mean fields and energies. The differences between the centroids obtained with T26, T44 and T62 are predominantly a consequence of the readjustment of the entire energy functional for each strength of the tensor terms.

The larger impact of the tensor terms on the  $1f$  levels than on the  $2p$  ones is still more apparent when a trivial angular-momentum factor in the spin-orbit splitting  $\Delta\epsilon_\ell$  is taken out. This result has a geometrical origin discussed in Fig. 16 of Article I for a different example: a zero-range tensor interaction has the largest impact on spin-orbit splittings for those levels that have the same nodal structure as the ones that dominate the spin-current  $\mathbf{J}$ .

As discussed in Article I and exemplified in Fig. 4, the isoscalar tensor term has the tendency to reduce the spin-orbit splitting in spin-unsaturated nuclei for the  $TIJ$  parameterizations studied here. To maintain a given splitting, the spin-orbit coupling constant has to be increased. Thus, the reduction of the spin-orbit splittings obtained with T44, as compared to those from T22, results from the partial compensation of the change in tensor and spin-orbit contributions. By contrast, the spin-orbit splittings obtained with T26, T44 and T62 are fairly independent on the value of the isovector tensor coupling constant  $C_1^J$ . The reason is twofold: on the one hand, the isovector spin-current tensor density is negligibly small in an  $N = Z$  nucleus and all direct isovector contributions to the spin-orbit field are suppressed. On the other hand, changing  $C_1^J$  in the fit does not induce a significant change of the strength of the spin-orbit interaction within the protocol of the  $TIJ$  interactions.

The values obtained with SLy5 and SLy5+T are listed in the next two lines of Table II. The negative value chosen for  $C_0^J$  in SLy5+T, is not compensated by a readjustment of the spin-orbit strength and leads to a substantial increase of all spin-orbit splittings. The negligible changes in the position of the centroids gives an indication of the order of magnitude of rearrangement effects from self-consistency.

The results obtained with SLy4, SLy4T, SLy4T<sub>min</sub>,

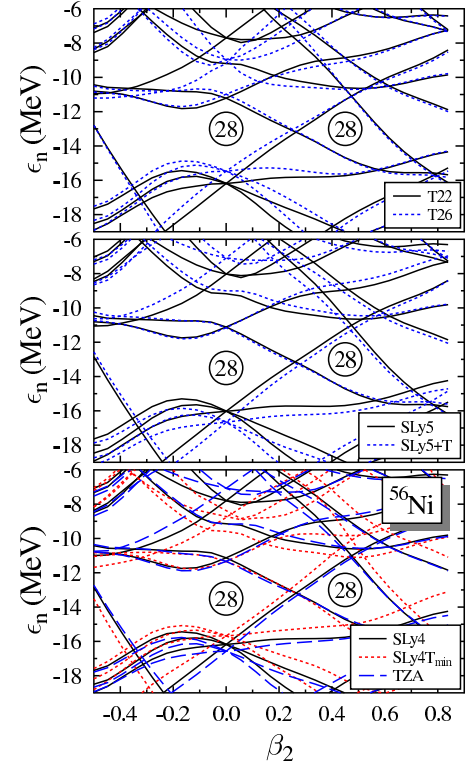


FIG. 7: (Color online) Neutron Nilsson single-particle diagrams for  $^{56}\text{Ni}$  obtained using various families of parameterizations (see text).

SLy4T<sub>self</sub> and TZA can be found in the last five lines of Table II. Although the tensor coupling constants of SLy4T and SLy5+T are similar, cf. Fig. 1, their behavior with respect to the parameterizations from which they have been constructed is quite different. The spin-orbit splitting of the  $1f$  levels obtained with SLy5+T is much larger than with SLy5, while that of SLy4T is smaller than that of SLy4. The good agreement with experiment obtained with SLy4T is not surprising since  $^{56}\text{Ni}$  is one of the data that has been used to adjust the spin-orbit and tensor strengths. The origin of the differences between these interactions is the additional reduction of the spin-orbit force in SLy4T, to about 2/3 of its original value. For  $^{56}\text{Ni}$ , the reduced spin-orbit interaction of SLy4T overcompensates the effect of the tensor interaction. The single-particle spectra obtained with SLy4T, SLy4T<sub>min</sub>, and SLy4T<sub>self</sub> differ slightly, which results from self-consistency in the calculations and the readjustment of the other coupling constants of the functional. Since TZA has the same tensor coupling constants as SLy4T, but an increased spin-orbit interaction, it predicts too large spin-orbit splittings.

The single-particle spectra from SLy4 and T22, obtained from almost the same fit protocol, are very close as should be expected. Also, the single-particle spectrum obtained with SLy4 lies in between those from SLy5 and SLy5+T, as could be expected from their tensor coupling



constants, Fig. 1, and the similarities of the respective fits.

Comparing calculated single-particle energies to empirical ones from [37] and to experimental separation energies, the fine tuning of the spin-orbit splittings that constitutes the main difference between the interactions studied here does not significantly improve the overall agreement with data. The main deficiency shared by all parameterizations is that the relative distance between the centroids of the  $1f$  and  $2p$  levels is nearly 2 MeV too small, leading to different sequences of the  $1f_{5/2}$ - and  $2p_{1/2}$ - levels in calculations and data. This result is consistent with the suspicion raised in Ref. [40] that a substantial increase of the distance between the centroids given by SLy4 might be needed to reproduce the shape coexistence phenomena around  $^{74}\text{Kr}$ . However, a more careful analysis of the physics that connects the single-particle spectra and the observable separation energies is needed before a final conclusion can be drawn.

### 5. Nilsson diagrams

At sphericity, the single-particle spectra obtained with interactions adjusted using the same protocol exhibit minor differences, with a splitting of the  $1f$  levels varying by about 250 keV. Variations are slightly larger when the tensor term is added perturbatively. The effects of these differences on the dependence of the single-particle levels on deformation can be found in Fig. 7. Two  $TIJ$  parameterizations only are plotted, as the results do not depend on the isovector coupling constant  $C_1^J$ . Nilsson diagrams for protons differ mainly by a constant shift due to the Coulomb interaction.

The most striking insight from Fig. 7 is that changing the strength of the isoscalar tensor coupling modifies the slope of the level dependence on deformation, especially close to sphericity. The impact on deformed shell gaps depends, however, on how a tensor term has been introduced.

For refitted parameterizations such as T22 and T26, the difference between the position of the  $1f_{7/2}$ - levels at sphericity is compensated by the change of the slope of the single-particle levels in such a way that the gap at  $\beta_2 = 0.5$  has about the same size. A similar result is obtained for all  $TIJ$  and SLy $x$  parameterizations.

In contrast, for interactions with perturbatively added or rescaled terms, the size of the deformed gap is strongly modified: it becomes smaller for SLy5+T, and larger for SLy4T<sub>min</sub>. The origin of the latter difference is the reduced spin-orbit interaction for SLy4T<sub>min</sub>. With the same tensor coupling constants as SLy4T<sub>min</sub>, TZA leads to results similar to those of the  $TIJ$  parameterizations.

Similar results and similar observations can be made are obtained for all other nuclei discussed hereafter.

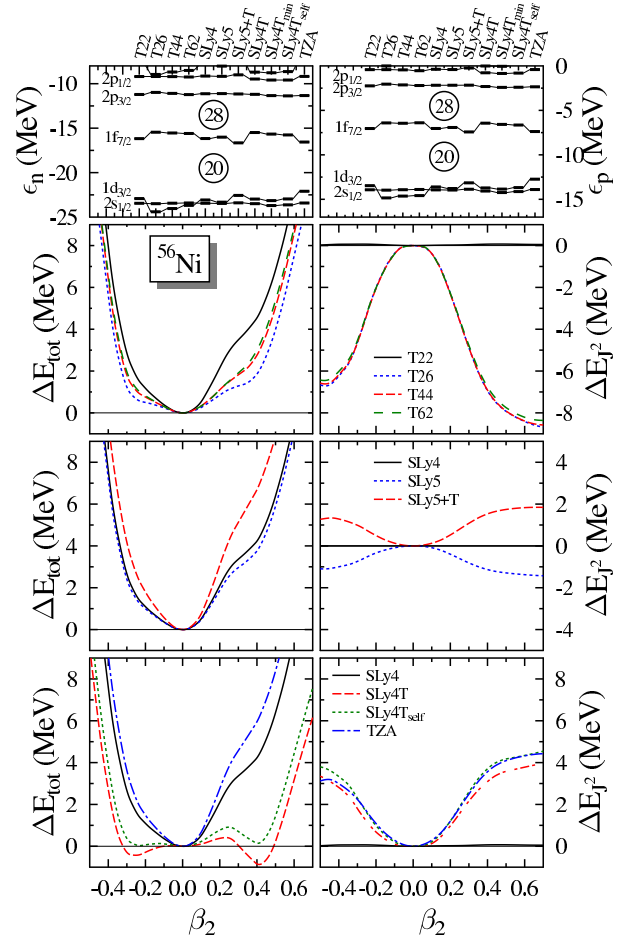


FIG. 8: (Color online) The single-particle spectra at spherical shape are shown in the upper panel for neutrons (left) and protons (right). The deformation energy (left) and the variation of the total tensor energy (right) are plotted on the lower panels for  $^{56}\text{Ni}$  and different Skyrme parameterizations, as indicated.

### 6. Deformation energy and its tensor term contribution

Deformation energy curves are plotted in Fig. 8. To facilitate their correlation with shell structure, the corresponding neutron and proton single-particle spectra at sphericity are given in the upper panels. The total deformation energy is given on the left-hand-side in the lower panels, whereas the difference between the tensor energy contribution at a given deformation and at sphericity is provided on the right-hand-side. This tensor energy contribution decreases with deformation for  $TIJ$  parameterizations and for SLy5, for which  $C_0^J$  is positive. It increases for the other parameterizations that have a negative  $C_0^J$ .

The differences between the energy curves are not directly linked to the evolution of the tensor energy. They can, in fact, be related to the shell effects that are seen in Fig. 7 and, in particular, to the relative size of the spherical and prolate deformed  $N = Z = 28$  gaps. A

well-defined spherical minimum and a pronounced shoulder at a deformation around  $\beta_2 = 0.5$  are obtained for SLy4, SLy5 and the  $TIJ$  parameterizations. This structure in the energy curve is at a position qualitatively in agreement with the properties of a superdeformed rotational band observed in  $^{56}\text{Ni}$  [38].

The combined effect of the reduced spherical  $N = Z = 28$  gap and the large deformed gap obtained with SLy4T has the unphysical consequence that the ground state corresponds to a superdeformed minimum. This result is related to a deficiency of SLy4 on which the tensor interaction has no effect. This interaction, indeed, predicts too small a distance between the centroids of the  $1f$ ,  $2p$  orbitals (see Table II). In such a case, reproducing the empirical data for the splitting of the  $1f$  levels does not guarantee a realistic shell structure. In practice, the gap between the  $1f_{7/2-}$  and  $2p_{3/2-}$  levels becomes too small, whereas the distance between the  $1f_{7/2-}$  and  $1g_{9/2+}$  levels is now too large.

The parameterization SLy5+T has the inverse drawback: the gap at 28 is too large at sphericity, preventing the formation of a secondary gap at large deformation.

The deformation energy and the relative change of the tensor terms obtained with SLy4T (shown) and with SLy4T<sub>min</sub> (not shown) cannot be distinguished within the resolution of Fig. 8. This is less obvious than one might think. The refit that leads from SLy4T to SLy4T<sub>min</sub> changes the absolute binding energy of  $^{56}\text{Ni}$  by nearly 6 MeV from  $-469.522$  (SLy4T) to  $-475.480$  MeV (SLy4T<sub>min</sub>).

The results obtained with SLy4T<sub>self</sub> and TZA confirm the crucial role of the spin-orbit strength. Both interactions have been adjusted with the same protocol and the SLy4T values for the tensor coefficients, but SLy4T<sub>self</sub> shares the same spin-orbit strength as SLy4T while it has been freely varied for TZA. This variation of the spin-orbit leads to results quite close to those of the  $TIJ$  parameterizations for TZA, in contrast to what is obtained with SLy4T<sub>self</sub>.

### 7. The freedom of using an energy density functional

As discussed in Sect. III, the fits of tensor couplings have all been performed assuming spherical symmetry. Two coupling constants have been fixed in this way, either  $t_e$  and  $t_o$  or  $C_t^{J1}$ ,  $t = 0, 1$ . There remains the freedom to choose the  $C_t^{J2}$  coefficients. It has been assumed, for the interactions  $TIJ$ , that there are underlying two-body central, spin-orbit and tensor forces, cf. Sect. IID. In this case, there is a one-to-one correspondence between the  $C_t^{J1}$  coefficients and parameters  $t_1$ ,  $x_1$ ,  $t_2$ ,  $x_2$  of the central Skyrme force and parameters  $t_e$  and  $t_o$  of the tensor force. With this choice, all coupling constants of the energy functional,  $C_t^{J2}$ ,  $t = 0, 1$ , or, alternatively, the  $C_t^T$  and  $C_t^F$  coupling are also fixed. As explained in Sect. IID, other choices can be made. To explore the impact of doing so, we have constructed three variants

TABLE III: Tensor coupling constants of T44 and three extensions of T44 beyond the spherical symmetry constructed using the freedom of choice given by an energy functional (see text). All values are in MeV fm<sup>5</sup>. Coupling constants are given for all three representations of the tensor part of the energy functional, Eqns. (11) and (16). All coupling constants not shown are identical.

	T44	T44 II	T44 III	T44 IV
$C_0^{J0}$	-20.994	-60	40	-160
$C_1^{J0}$	50.027	0	0	0
$C_0^{J1}$	60	60	60	60
$C_1^{J1}$	0	0	0	0
$C_0^{J2}$	46.806	0	120	-120
$C_1^{J2}$	62.433	0	0	0
$C_0^T$	-83.403	-60	-120	0
$C_1^T$	-31.216	0	0	0
$C_0^F$	73.194	120	0	240
$C_1^F$	-62.433	0	0	0
$b_{14}$	52.187	60	120	0
$b_{15}$	62.433	0	0	0
$b_{16}$	-67.813	-60	0	-120
$b_{17}$	62.433	0	0	0

of the parameterization T44, listed in Table III. These consist of setting either  $C_0^{J2}$  (case II), or  $C_0^F$  (case III), or  $C_0^T$  to zero (case IV). Each choice leads to different values for the coupling constants of the pseudoscalar and pseudotensor part of the tensor terms. We concentrate here on the isoscalar part of the functional, since for the purpose of our study isovector effects are negligible in a  $N = Z$  nucleus.

The total deformation energy and the variation of tensor contributions with respect to their value at sphericity are plotted in Fig. 9 as a function of deformation. The total tensor energies (bottom left), and the decomposition into vector and pseudotensor contributions on the one hand (top), and into symmetric and asymmetric cartesian components on the other hand (middle) are presented.

As expected from the smallness of the pseudotensor contribution in Fig. 6, the choice II where the coefficient  $C_0^{J2}$  is set to zero does not lead to any sizable difference with T44. The results for the two other choices are less obvious. As can be seen on the middle panels of Fig. 9, the cartesian components of the tensor energy are both sizable and one could expect that setting one of the two coefficients of these terms to zero will have a large effect. One can see in the middle panels of Fig. 9 that both terms show significant variation with respect to deformation. The decomposition is even significantly different for T44 and choice II, although leading in both cases to the same total energy. Self-consistency effects are such that for the choices III (where  $J_{q,\mu\nu}J_{q,\nu\mu}$  has a coefficient equal

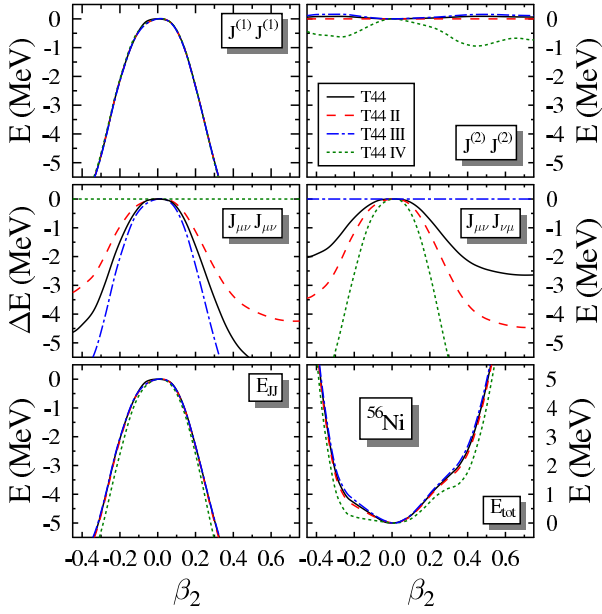


FIG. 9: (Color online) Deformation energy curve (lower right), tensor energy (lower left), and its decomposition into symmetric, asymmetric, vector and pseudotensor parts for  $^{56}\text{Ni}$  as obtained with the variants of T44 defined in Table III.

to zero) and IV (where  $J_{q,\mu\nu}J_{q,\mu\nu}$  has a coefficient equal to zero), the remaining contribution has a variation very similar to the variation of the total tensor energy of T44.

The way a parameterization is extended beyond sphericity has a small, but visible, effect on the variation of the total energy with deformation. Setting the coefficient of  $J_{q,\mu\nu}J_{q,\mu\nu}$  equal to zero, (option IV) significantly softens the energy curve with an oblate shoulder nearly degenerate with the spherical configuration. The extension of a parameterization beyond sphericity is not a trivial choice and the procedure followed for such extension should always be made transparent. The small differences seen in a simple nucleus such as  $^{56}\text{Ni}$  could become more dramatic in other nuclei.

#### D. Doubly-magic nuclei

##### 1. $^{40}\text{Ca}$

The  $N = Z = 20$  nucleus  $^{40}\text{Ca}$  is the heaviest known doubly-magic nucleus which exhibits oscillator shell closures. The variation of the total energy, the change of the contribution to the energy of the tensor terms, and the single-particle spectra at spherical shape are plotted in Fig. 10. The configuration of  $^{40}\text{Ca}$  is spin-saturated at sphericity, and the corresponding tensor energy is only due to small effects as pairing and non-identity of the single-particle wave functions of spin-orbit partners. Spin saturation disappears as soon as the nucleus is deformed, but the filling of single-particle states remains identical for protons and neutrons. Thus, the contribution of the

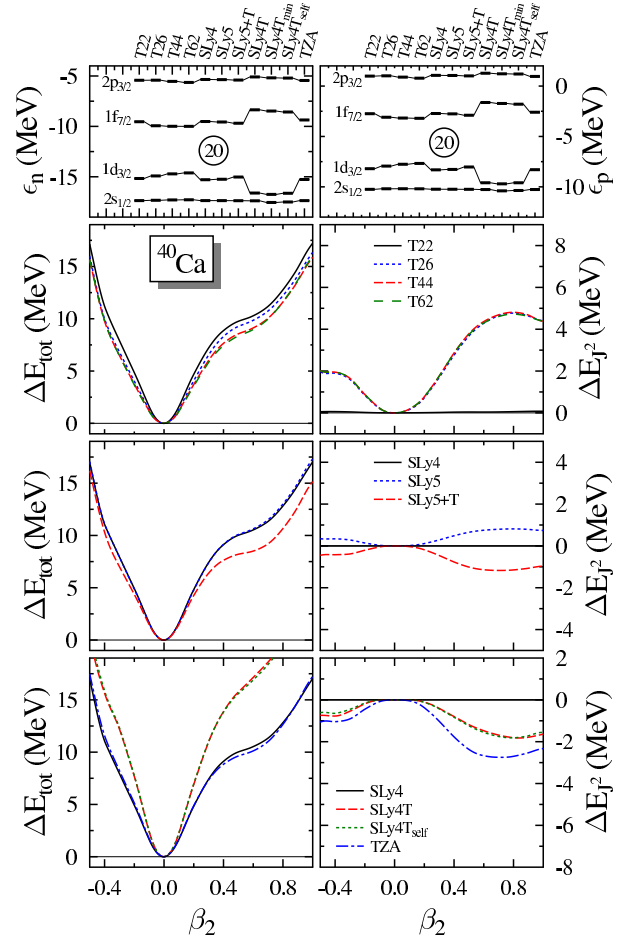


FIG. 10: (Color online) Same caption as Fig. 8, but for  $^{40}\text{Ca}$ . Note that the scale of the total deformation energy differs from the one of the tensor terms by a factor two.

tensor terms to the total binding energy induced by deformation is almost purely isoscalar and has the same sign as the isoscalar coupling constant  $C_0^J$ . The tensor term is close to zero at sphericity, and increases with deformation. As the coupling constant  $C_0^{J1}$  of the isoscalar vector part of the tensor terms is the same for T26, T44 and T62,  $C_0^J = 120 \text{ MeV fm}^5$ , these interactions give nearly identical tensor contributions to the total energy.

Despite this feature, the energy curves corresponding to T26, T44 and T62, are not identical. One can see that the softness of the energy curves increases with the strength of the isovector part of the tensor interaction. Once again, these changes result from the readjustment of the coupling constants of all terms of the energy functional when varying  $C_0^J$  and  $C_1^J$  to a sample of data that includes both  $N = Z$  and  $N \neq Z$  nuclei. In fact, as for  $^{56}\text{Ni}$  discussed in Figs. 3 and 4, most components of the energy show larger variations between the parameterizations than the tensor energy. This example illustrates particularly well the fact that the impact of the tensor terms on deformation energies cannot be foreseen from the sole knowledge of the tensor coupling constants and of

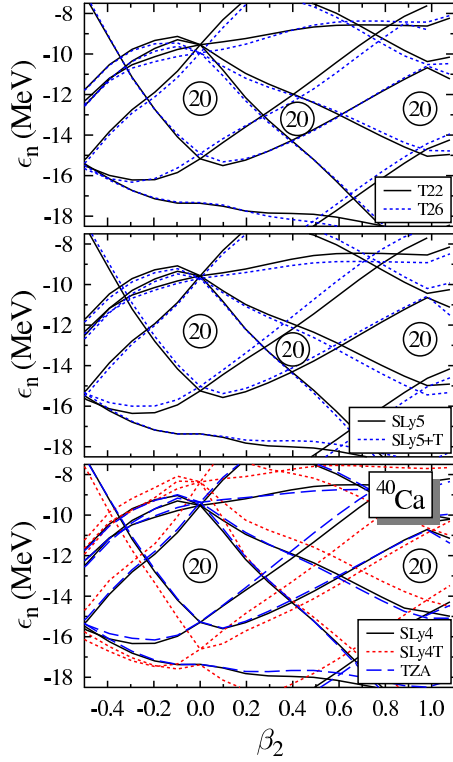


FIG. 11: (Color online) Same as Fig. 7, but for  $^{40}\text{Ca}$

the variation of the degree of spin saturation with deformation. The energy of the shoulder that can be seen at a  $\beta_2$  value around 0.5 is significantly lowered for the tensor interactions T44 and T62. This shoulder can be related to the existence of a superdeformed band in  $^{40}\text{Ca}$  [41, 42].

The isoscalar tensor coupling is attractive for SLy5+T and SLy4T. The energy curve obtained with SLy5+T is only slightly different from the one calculated with SLy5 around sphericity, but presents a significant lowering of the energy of the shoulder. The situation is quite different for SLy4T. The energy curve varies in opposite direction from the tensor energy and is stiffer than that obtained with SLy4. In particular, the shoulder is obtained at a much larger excitation energy. This clearly is a consequence of the reduced spin-orbit interaction, as this feature of SLy4T is shared by SLy4T<sub>self</sub>, but not TZA. The energy of the tensor term is larger for the parameterization TZA than for SLy4T, although the tensor coefficients have the same values in both cases. The increase (in absolute value) of the tensor energy is compensated by changes in other terms of the energy functional, in particular a slight reduction of the spin-orbit term, in such a way that the energy curves obtained with SLy4 and TZA are nearly undistinguishable.

The qualitatively different deformation dependence of the tensor energy found for  $^{56}\text{Ni}$  and  $^{40}\text{Ca}$  is accompanied by systematic differences in the single-particle levels given in Fig. 11. As  $^{40}\text{Ca}$  is spin-saturated, the spectrum at sphericity is nearly the same for all parameter-

izations, except SLy4T. The contributions of the tensor terms are indeed small, although not exactly zero. The largest differences between the results obtained with the  $TIJ$  parameterizations are those for T22 and T26. They are related to the slight difference between their coupling constants and, in particular, to the larger strength of the spin-orbit of T26 compared to T22, cf. Article I. This effect of the spin-orbit interaction on the single-particle levels is more drastic when its strength is explicitly adjusted to spin-orbit splittings in this mass region, as illustrated by the comparison between SLy4T and SLy4.

As for  $^{56}\text{Ni}$ , Fig. 7, the tensor interaction affects the slope of the single-particle levels shown in Fig. 11 as a function of deformation. However, the changes in slopes for a given parameterization are opposite for both nuclei. This is related to the difference in the tensor contribution to the spin-orbit field: it increases with deformation for  $^{40}\text{Ca}$ , while it decreases in  $^{56}\text{Ni}$ . The change in slope at least partly compensates the differences found at spherical shape when going to deformed ones. As a consequence, the spectra around the Fermi energy at large deformation are close for refitted parameterizations such as T22, T26 and TZA. On the contrary, the differences between the spectra for a perturbative interaction such as SLy5+T and the original one increases with deformation. Differences are larger at all deformations for SLy4T compared to SLy4 and TZA, as a consequence of a perturbative modification of the tensor and the spin-orbit parameterizations.

## 2. $^{48}\text{Ca}$

The  $Z = 20$ ,  $N = 28$  nucleus  $^{48}\text{Ca}$  is spin saturated in protons and unsaturated in neutrons at sphericity. The variations of the tensor energy and of the total energy with deformation are given in Fig. 12. The upper panels show that the four  $TIJ$  parameterizations behave very differently in contrast to the case of  $^{40}\text{Ca}$ . The tensor energy is nearly independent of deformation for T44, whereas it decreases with deformation for T26 and increases for T62. As confirmed by the behaviors of the  $T = 0$  and  $T = 1$  components of the tensor energy that are plotted in Fig. 13, the isoscalar contribution to the tensor energy does not vary much for all  $TIJ$  parameterizations, whereas the isovector contribution presents an extremum at sphericity and goes rapidly to zero with deformation. One can relate the behavior of the tensor energy to the fact that the spin-current density is the largest for neutrons at sphericity, but nearly zero for protons. With increasing deformation the proton spin-current density grows, whereas the neutron one is reduced, as can be deduced from the decomposition of the tensor terms into their nn, pp and np contributions provided in Fig. 13. Note for T62 that the nn and pp contributions are close to zero at all deformations by construction, but this does not result in the proportionality of  $T = 0$  and  $T = 1$  components with respect to each other



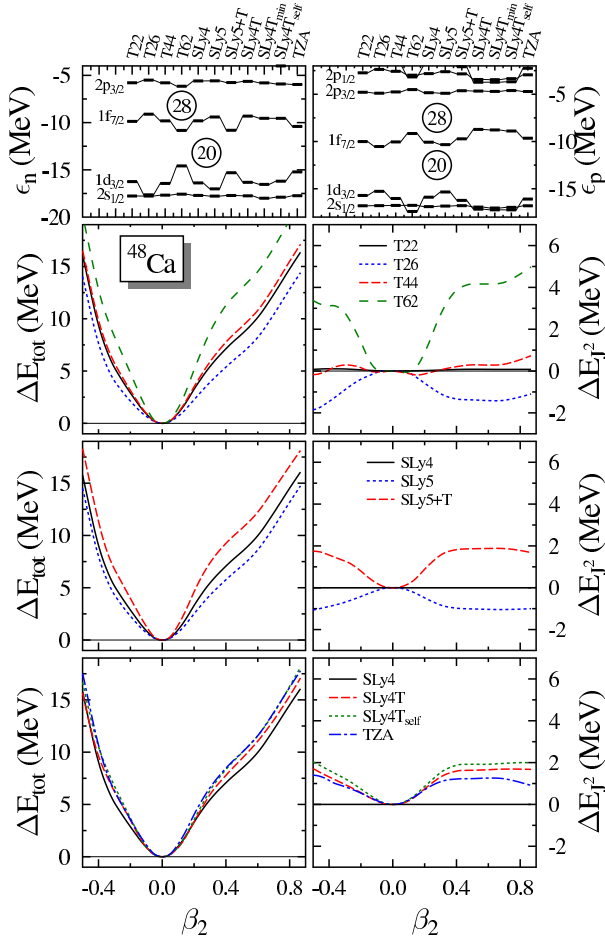


FIG. 12: (Color online) Same caption as Fig. 8, for  $^{48}\text{Ca}$ . Note that the scale of the total deformation energy differs from the one of the tensor terms by a factor two.

and to the np contribution. In general, the nn and pp contributions to both  $T = 0$  and  $T = 1$  part are nonzero and deformation dependent. Similarly, from the (by construction) nearly vanishing np contribution found at all deformations for T26 it also cannot be concluded that the  $T = 0$  and  $T = 1$  components are proportional to each other and the sum of the nn and pp contributions.

For  $^{48}\text{Ca}$ , the differences between the deformation energy curves in Fig. 12 are clearly correlated with the variations in the isovector tensor energy. The curve is softer for a repulsive isovector contribution to the tensor energy, as it is for T26, and stiffer for an attractive isovector contribution, as it is for T62. This counterintuitive outcome is the consequence of the rapid decrease of the isovector tensor energy from large values at sphericity to very small values with deformation, cf. Fig. 13. The results obtained with the interactions SLy4T and SLy5+T are plotted in the lower panels of Fig. 12. The isovector tensor term has the same sign for these two interactions as for T62 leading also to stiffer energy curves. However, the magnitude of the effect is smaller, the isovector coupling constants being smaller.

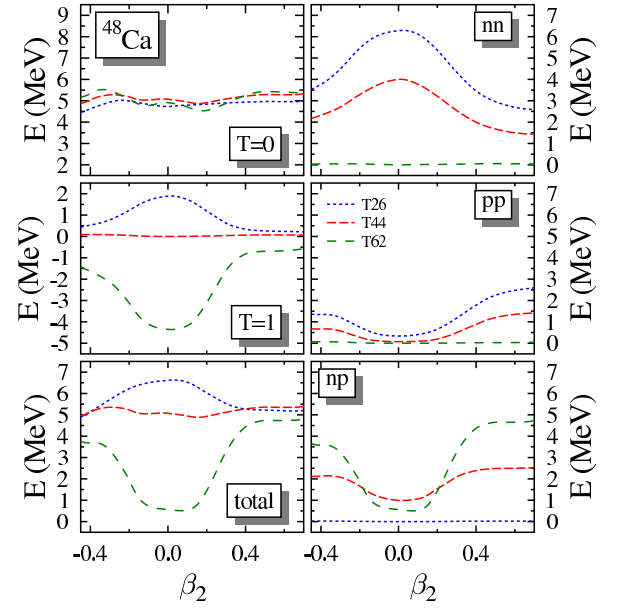


FIG. 13: (Color online) Decomposition of the total contribution of the tensor terms to the total energy (lower left) into its isoscalar ( $T = 0$ ) and isovector ( $T = 1$ ) parts (upper and middle left), and into its nn, pp and np contributions (right panels) for  $^{48}\text{Ca}$  and for the parameterizations T26, T44 and T62.

Compared to all other interactions, but T62, the SLy4T, SLy4T<sub>min</sub> and SLy4T<sub>self</sub> functionals give a larger  $Z = 20$  gap at the expense of a reduced  $Z = 28$  one. This is the consequence of the tightly adjusted spin-orbit splittings of the  $1f$  levels in  $^{40}\text{Ca}$ ,  $^{48}\text{Ca}$ , and  $^{56}\text{Ni}$  through an attractive tensor interaction in conjunction with a reduced spin-orbit force. The reduced spin-orbit interaction also switches the ordering of the  $1d_{3/2+}$  and  $2s_{1/2+}$  levels below the  $Z = 20$  gap, at variance with empirical data. Keeping the negative tensor coupling constants of SLy4T, but allowing for the readjustment of the spin-orbit strength in TZA brings the level spacings back to values close to the ones of the original SLy4 interaction.

### 3. $^{68}\text{Ni}$

It is usually assumed from its spectrum that  $^{68}\text{Ni}$  is doubly-magic [43, 44, 45]. The excitation energy of its first  $2^+$  state is, indeed, large and the  $B(E2; 0^+_{\text{gs}} \rightarrow 2^+_1)$  value small [46]. However, while the  $Z = 28$  proton shell closure is clearly visible in the mass systematics along the  $N = 40$  isotonic chain [47], there is no pronounced discontinuity in the masses of Ni isotopes when crossing  $N = 40$  [47, 48], which hints at a more complex situation. An alternative explanation of the properties of the first  $2^+_1$  state in  $^{68}\text{Ni}$  is based on the impossibility to construct the first  $2^+$  state as a simple neutron  $1p$ - $1h$  excitation. Indeed, the odd-parity  $pf$  shell is completely filled and the  $1g_{9/2+}$  orbital empty [49, 50] and at least a  $2p$ - $2h$



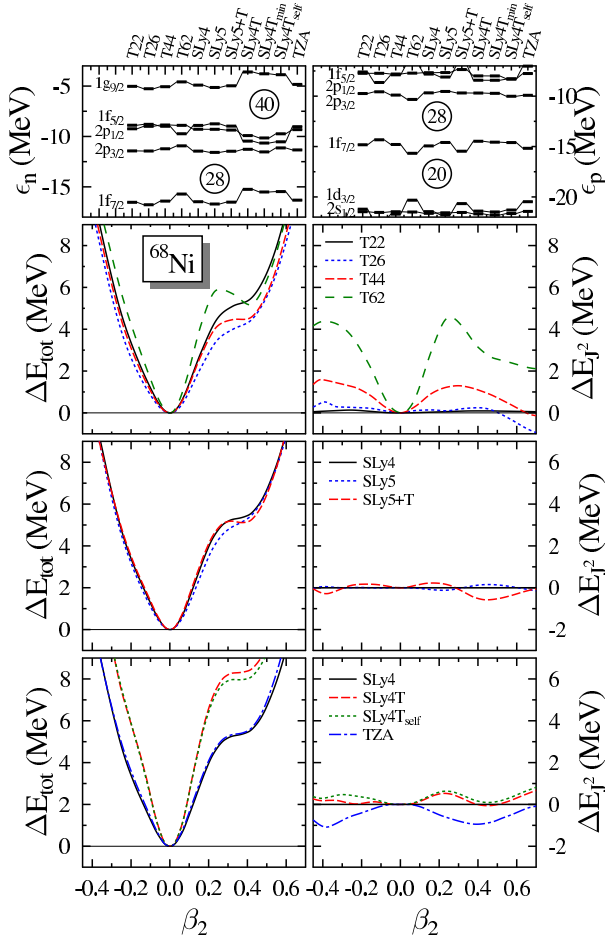


FIG. 14: (Color online) Same caption as Fig. 8, but for  $^{68}\text{Ni}$ .

excitation is needed to construct a positive-parity state. The interpretation of  $^{68}\text{Ni}$  as a doubly-magic nucleus has also been questioned by shell model and QRPA calculations [51]. Let us mention, finally, that the first excited state of  $^{68}\text{Ni}$  is a  $0^+$  level with a small  $B(E0)$  value to the ground state [52], pointing to a possible shape coexistence with weak mixing.

The deformation energy curves and the variation of the tensor energy with deformation are plotted in Fig. 14 for  $^{68}\text{Ni}$ . With  $N = 40$  and  $Z = 28$ , this nucleus is spin-saturated for neutrons and spin-unsaturated for protons.

It is instructive to compare  $^{68}\text{Ni}$  and  $^{48}\text{Ca}$  (Fig. 12). Both nuclei have, indeed, similar single-particle configurations. The  $1f_{7/2-}$  subshell is completely filled for protons in  $^{68}\text{Ni}$  and for neutrons in  $^{48}\text{Ca}$ , and both nuclei are spin-saturated for the other type of nucleons. However, the comparison of both nuclei in fact indicates large differences. The variance can be related to two factors. First, the degeneracy of the shells that makes the  $N = 40$  gap for neutrons is much larger than those that make the  $Z = 20$  gap for protons. Second, the  $Z = 20$  and  $N = 40$  gaps have different sizes. The latter is not large enough to suppress pairing correlations, such that the spin-saturation is broken and the neutron

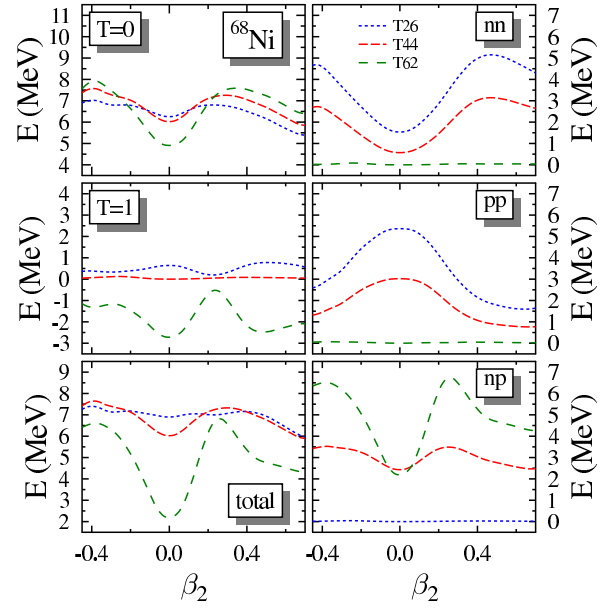


FIG. 15: (Color online) Same caption as Fig. 13, but for  $^{68}\text{Ni}$ .

spin-current density is non-negligible at spherical shape, in particular for the T26 parameterization predicting the smallest  $N = 40$  gap. The main consequence is that for  $^{68}\text{Ni}$  all contributions to the tensor energy at spherical shape are nonzero, unless suppressed by their coupling constant, see Fig. 15. Also, the np component is not just increasing with deformation but fluctuating, most obviously for T62, where it is the only sizable non-zero contribution. By contrast, the rapidly varying nn and pp contributions for T26 fortuitously add up such that this parameterization presents the smallest variation of the tensor energy among the parameterizations with the same isoscalar coupling constant. The behavior of the tensor energy is reflected in the total energy curves in Fig. 14: it creates an inflexion of the energy curve at  $\beta_2 \approx 0.4$ , which is sufficiently large for T62 to create a secondary minimum.

The tensor energy varies less with deformation for both the SLy5 and SLy5+T interactions; therefore, the energy curves obtained with both of these parameterizations and with SLy4 are very similar. The gap at  $N = 40$  obtained with SLy4T is larger, having the size of a major shell closure. It results in a very stiff energy curve. Such a behavior is not directly related to the variation of the tensor energy with deformation, but to the small spin-orbit strength, as shown by comparing the results of SLy4T<sub>self</sub> and TZA, just like for  $^{40}\text{Ca}$ .

#### 4. $^{78}\text{Ni}$

Although it has been observed for the first time more than a decade ago [53], not much is yet known about the neutron-rich  $^{78}\text{Ni}$  besides its existence and its  $\beta$ -decay half-life [54]. The relatively long half-life and the sys-

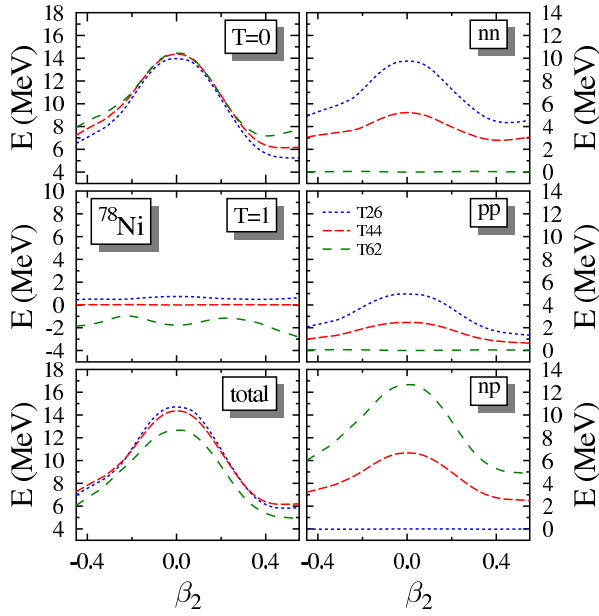


FIG. 16: (Color online) Same caption as Fig. 13, but for  $^{78}\text{Ni}$ .

tematics of the separation energies to and from  $N = 50$  isotones down to  $Z = 30$  suggests that the  $N = 50$  shell closure persists for  $^{78}\text{Ni}$  [55]. In such a case,  $^{78}\text{Ni}$  is spin non-saturated both in protons at  $Z = 28$  and neutrons at  $N = 50$ . The spin-currents from the unsaturated proton  $1g_{9/2+}$  and neutron  $1f_{7/2-}$  levels point into the same direction. Their degeneracies differ by only two, and their nodeless radial wave functions are sufficiently similar that their contributions to the isovector spin-current density nearly cancel. This suggests that the isovector tensor terms cannot play a decisive role in  $^{78}\text{Ni}$ , in spite of this nucleus' large isospin asymmetry. The isovector decomposition of the tensor terms for T26, T44 and T62 shown in Fig. 16 indeed confirms that the  $T = 1$  contribution is small for all deformations. The  $T = 0$  contribution dominates and is nearly the same for all three parameterizations, such that the different relative weight of the nn, np and pp contributions does not play a significant role. One can, therefore, expect that its energy curves depend on the tensor parameterization in a way similar to  $^{56}\text{Ni}$ . Figure 17 indicates that this is, indeed, the case for all the interactions that we have studied. In particular, all interactions predict the behavior of a doubly-magic nucleus. The  $T/J$  parameterizations with non-zero  $C_0^J$  values lead to softer energy curves than T22, SLy4 and SLy5, with an inflexion point around  $\beta_2 = 0.3$ , whereas SLy5+T gives a much stiffer deformation energy curve. The difference between the total deformation energy curves from T26, T44 and T62 is even smaller for  $^{78}\text{Ni}$  than what was found for  $^{56}\text{Ni}$ . This suggests that the readjustment and self-consistency effects at its origin for  $^{56}\text{Ni}$  are compensated by the asymmetry in  $^{78}\text{Ni}$  just in such a way that the net isospin dependence vanishes for this nucleus.

The parameterizations SLy4T and SLy4T<sub>self</sub> give again

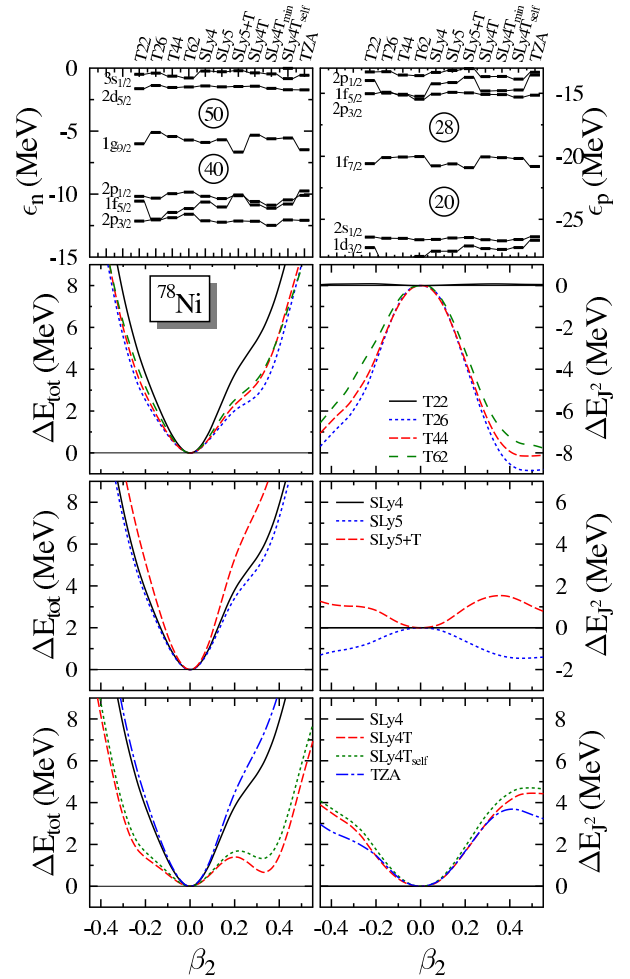


FIG. 17: (Color online) Same caption as Fig. 8, for  $^{78}\text{Ni}$ .

results that are qualitatively different from those of the others: they lead to a very pronounced deformed minimum at an excitation energy around 1 MeV, although the spherical gaps at  $N = 50$  and  $Z = 28$  are not smaller than those from T26, for example. This is again a consequence of the reduced contribution of the spin-orbit interaction to the deformation energy for these interactions.

## 5. $^{100}\text{Sn}$

The proton-rich and probably heaviest bound  $N = Z$  doubly-magic nucleus  $^{100}\text{Sn}$  has been observed more than a decade ago [56, 57]. Up to now, the only spectroscopic information in the direct vicinity of the nucleus is a 172 keV  $\gamma$  ray observed in  $^{101}\text{Sn}$  [58]. It has been tentatively interpreted as corresponding to the transition between an excited  $7/2^+$  level to the  $5/2^+$  ground state although the order of these two levels is not firmly established. In any case, the distance between these two levels is much lower than the energy difference between the spherical  $1g_{7/2+}$  and  $2d_{5/2+}$  orbitals predicted by all Skyrme parameter-

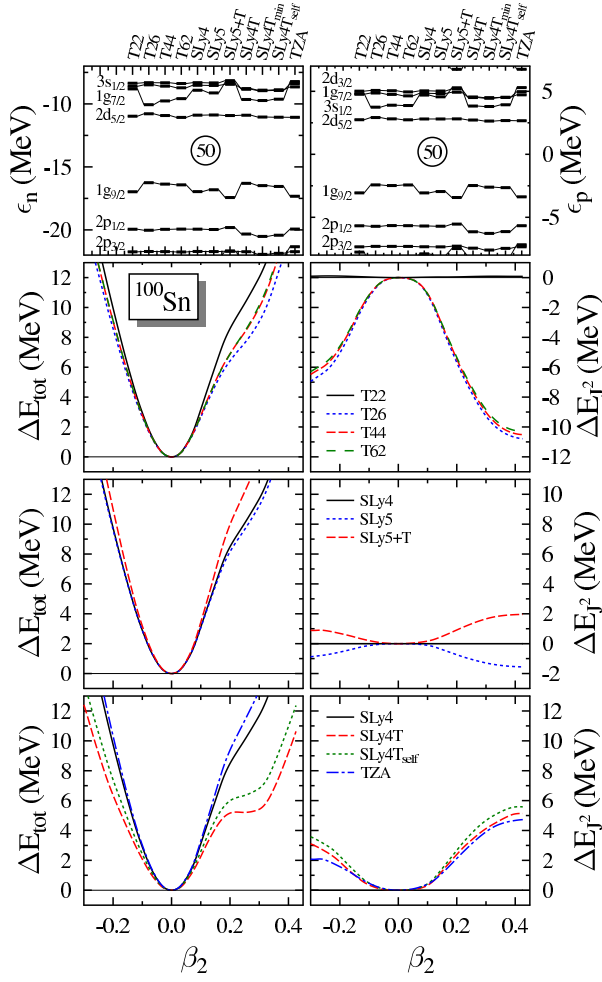


FIG. 18: (Color online) Same caption as Fig. 8, but for  $^{100}\text{Sn}$ .

izations plotted in Fig. 18. The tensor interaction has some effect on this spacing: it decreases from more than 1 MeV for T22 down to 600 keV for T26. Of course, the comparison between the energy levels in  $^{101}\text{Sn}$  and the single-particle energies supposes that both are pure single-particle configurations which is far from being established. Similar discrepancies with other parameterizations of the self-consistent mean field were reported in Ref. [58]. From this, however, one cannot safely draw the conclusion that T26 is the most realistic among the parameterizations studied here. The distance between the  $1g_{7/2+}$  and  $2d_{5/2+}$  levels depends on the balance between the distance of the centroids of the  $1g$  and  $2d$  levels as well as on their respective spin-orbit splittings, none of which can be expected to be described well throughout the chart of nuclei for any of the current parameterizations of the Skyrme EDF, see Article I and [12].

The variation of the deformation energy and of the energy contribution of the tensor terms with quadrupole deformation for  $^{100}\text{Sn}$  are presented in Fig. 18. For all parameterizations, the results are very similar to those obtained for  $^{56}\text{Ni}$ , Fig. 8, and  $^{78}\text{Ni}$ , Fig. 17. The main

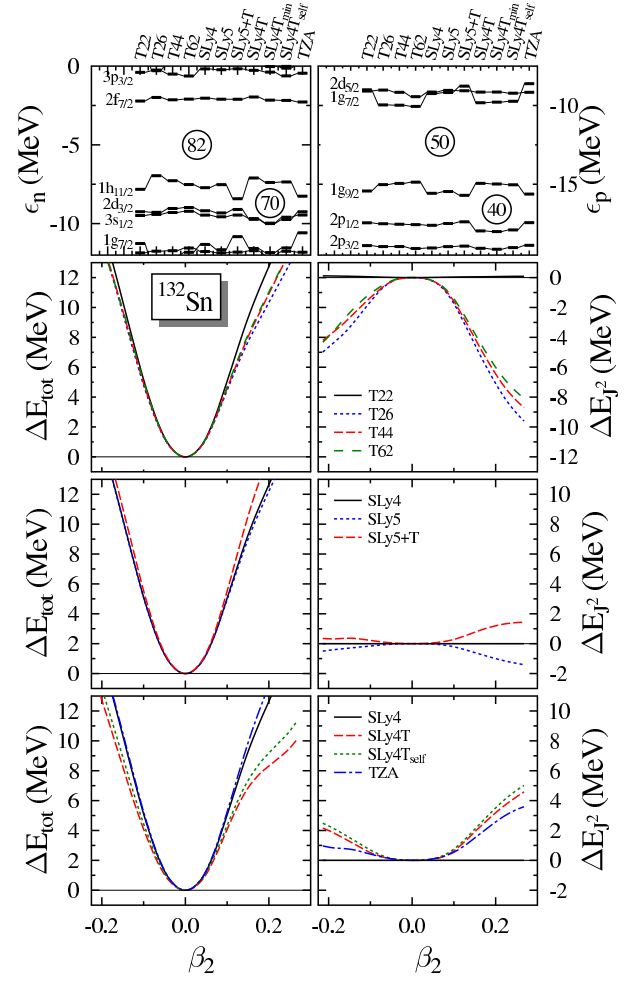


FIG. 19: (Color online) Same caption as Fig. 8, but for  $^{132}\text{Sn}$ .

difference is that the structure appearing at moderate deformation in the total deformation energy surface is less pronounced and located at higher excitation energies.

## 6. $^{132}\text{Sn}$ and $^{208}\text{Pb}$

The results obtained for the two heavy doubly-magic nuclei  $^{132}\text{Sn}$  and  $^{208}\text{Pb}$  are presented in Figs. 19 and 20. All neutron single-particle spectra exhibit the usual problem of all mean-field interactions that the  $1h_{11/2}$  level in  $^{132}\text{Sn}$  is not intruding the  $gds$  shell [2], as suggested by empirical data. The overall behavior of the energy curves below 8 MeV is very similar for most interactions. The stiffness of the deformation energy is marginally modified by the tensor interaction and much less than one might have expected from the variation of the single-particle spectra. The  $TIJ$  interactions with  $C_0^J$  coefficients different from zero give slightly softer deformation energy curves than T22 or SLy4. However, the dependence of the relative tensor energy on the value of the isovector coupling constant  $C_1^{J1}$  is very small for all de-

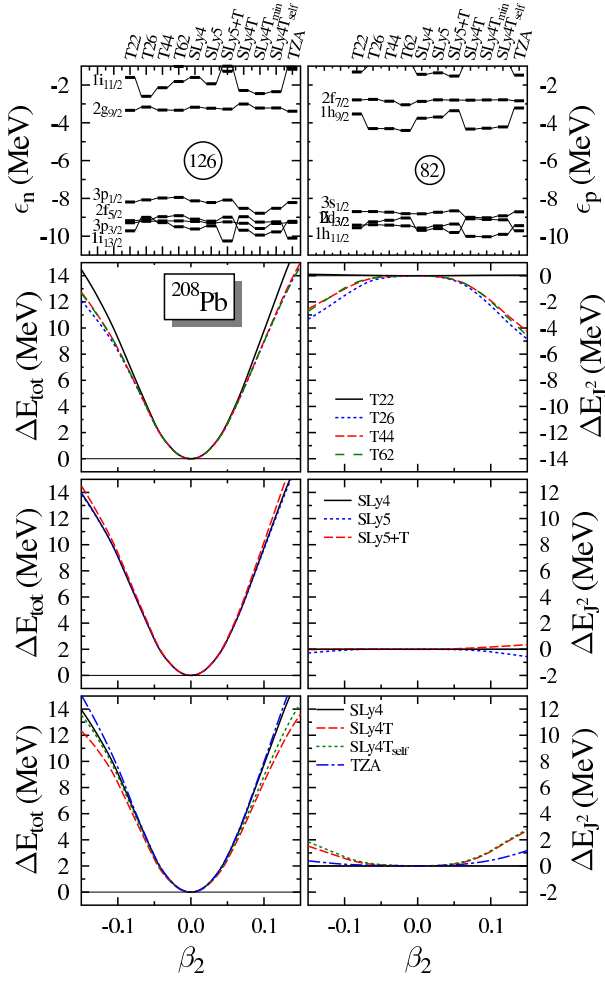


FIG. 20: (Color online) Same caption as Fig. 8, but for  $^{208}\text{Pb}$ .

formations for the same reason as for  $^{78}\text{Ni}$ , in spite of the large asymmetry of both nuclei. The reduction of the spin-orbit strength for SLy4T and SLy4T<sub>self</sub> leads to a prolate shoulder at about 10 MeV excitation energy. As already found for lighter nuclei, the variation of the tensor energy as a function of deformation can be large, up to 8 MeV in  $^{132}\text{Sn}$  and 4 MeV in  $^{208}\text{Pb}$  for the rather small range of deformations covered in Figs. 19 and 20. This significant variation is, to a large extent, absorbed by the rearrangement of the other terms of the Skyrme functional, and it does not affect significantly the total energy curves. The same mechanism that suppresses the isovector tensor terms for  $^{78}\text{Ni}$  is also at play in  $^{132}\text{Sn}$  and  $^{208}\text{Pb}$ ; hence, the variation of the tensor and total energy with deformation of both nuclei is mainly correlated with the isoscalar tensor coupling constant  $C_0^J$ .

### E. Selected Zr isotopes

The Zr,  $Z = 40$ , isotopic chain exhibits a rich spectroscopy, the neutron-deficient and neutron-rich isotopes

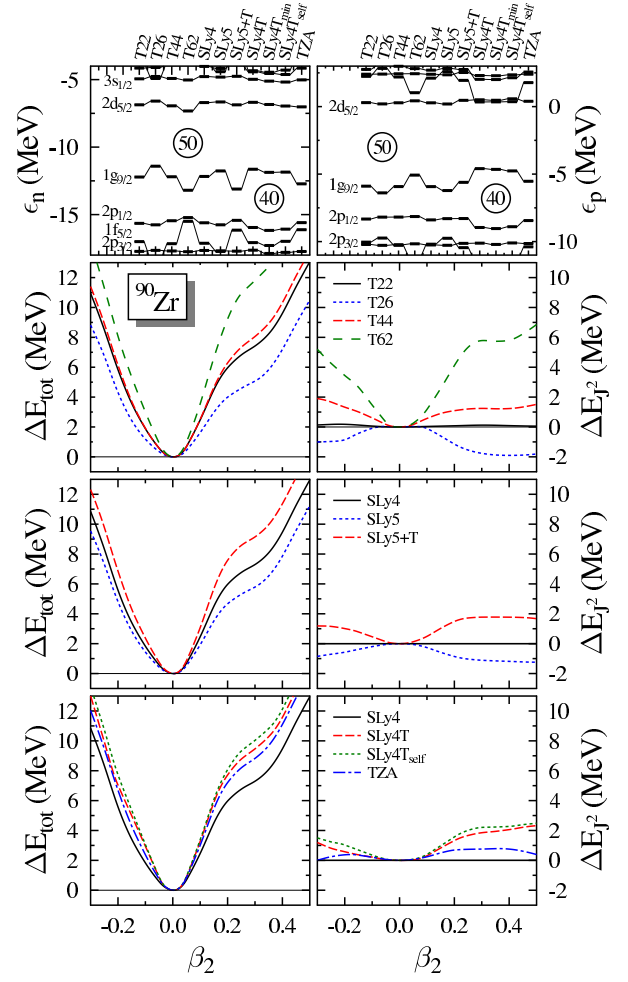


FIG. 21: (Color online) Same caption as Fig. 8, but for  $^{90}\text{Zr}$ .

being very deformed and the stable ones being spherical [59]. Self-consistent mean-field methods experience large difficulties to reproduce these very rapid variations of shapes in detail [21, 60, 61].

#### 1. $^{90}\text{Zr}$

The deformation energy and variation of the tensor contribution with quadrupole deformation for  $^{90}\text{Zr}$  are given in Fig. 21. There is a very close similarity between the results obtained for  $^{90}\text{Zr}$  and those for  $^{48}\text{Ca}$ , see Fig. 12. In both cases, protons are spin-saturated at sphericity whereas neutrons are non-saturated as they fully occupy the lowest shell of a pair of spin-orbit partners.

#### 2. $^{80}\text{Zr}$

The situation is different for the  $N = Z = 40$  isotope  $^{80}\text{Zr}$ . In spite of its double subshell closure, the

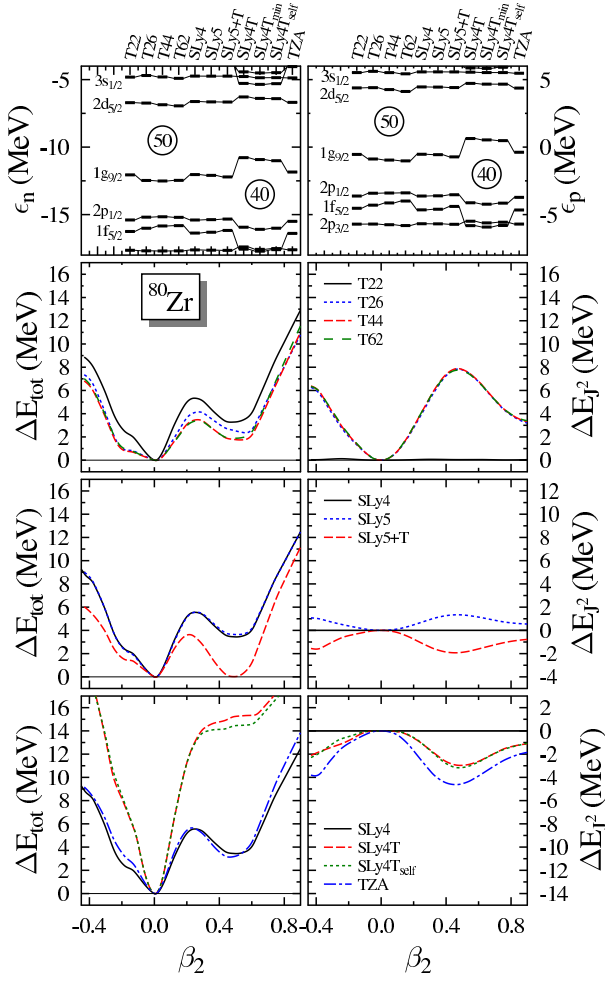


FIG. 22: (Color online) Same caption as Fig. 8, but for  $^{80}\text{Zr}$ .

sparse available spectroscopic data suggest that  $^{80}\text{Zr}$  has a large quadrupole deformation with a  $\beta_2$  value around 0.4. A rotational band built on the ground state has been observed up to a spin of  $10\hbar$  [62, 63, 64], although it appears to be slightly distorted at low spin. The large deformation of states in  $^{80}\text{Zr}$  is also supported by the observation of strongly-coupled rotational bands built on several Nilsson states in adjacent  $^{79}\text{Y}$  [65] and  $^{81}\text{Zr}$  [66]. In the absence of information on the transition matrix elements at the bottom of the band in  $^{80}\text{Zr}$ , however, it is not ruled out that spherical and deformed configurations might coexist in this nucleus and are strongly mixed in the ground state.

The deformation energy curves can be seen in Fig. 22. Protons and neutrons are spin-saturated at sphericity. As a consequence, the predicted properties of this nucleus present similarities with those of  $^{40}\text{Ca}$ : the energy of the tensor terms obtained using the T26, T44 and T62 interactions is very similar as only the isoscalar part of the tensor terms gives a sizable contribution. The total deformation energy, however, does exhibit a weak dependence on the value of  $C_1^{J1}$ . Also, comparing T22 and the

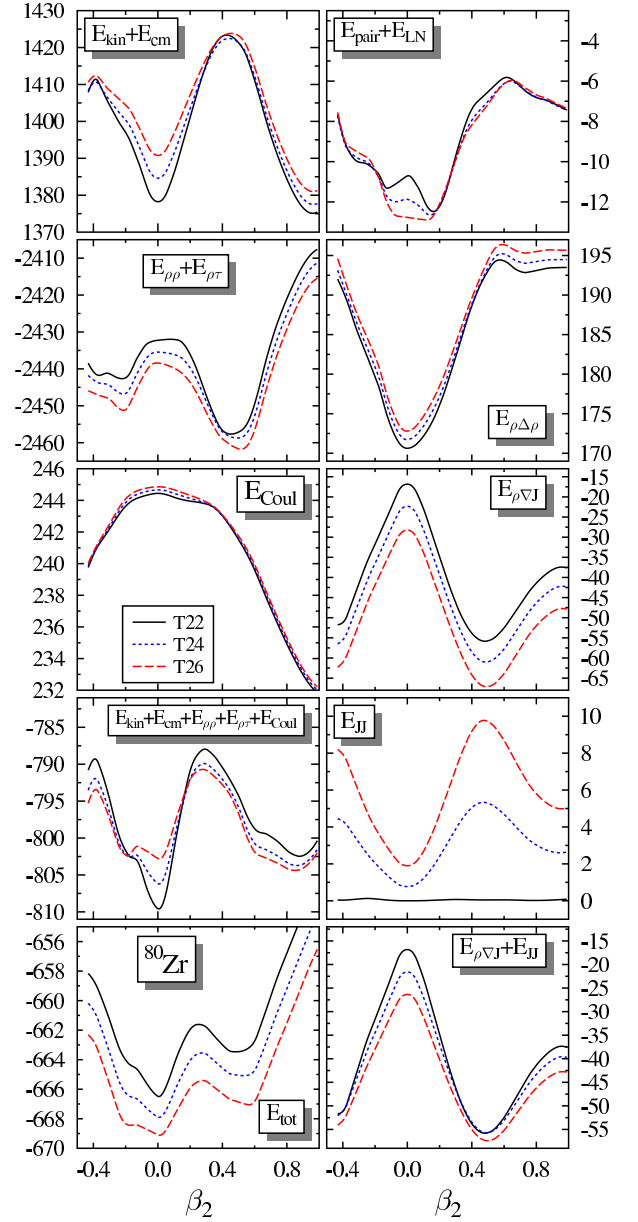


FIG. 23: (Color online) Same caption as Fig. 3, for  $^{80}\text{Zr}$ .

other  $T1J$  interactions, the variation of the tensor terms with deformation is in opposite direction to that of the total energy. Both results illustrate the importance of the changes induced in all terms of the functional by the fitting procedure.

The situation is different for interactions obtained by a perturbative procedure. In this case, the addition of a tensor term to an existing parameterization leads to more drastic changes. This is illustrated by the comparison between the energy curves obtained with SLy5 and SLy5+T. For the latter, the deformed minimum is pulled down and becomes degenerate with the spherical configuration. The situation is opposite for SLy4 and SLy4T. The large gap obtained with SLy4T for  $Z = N = 40$



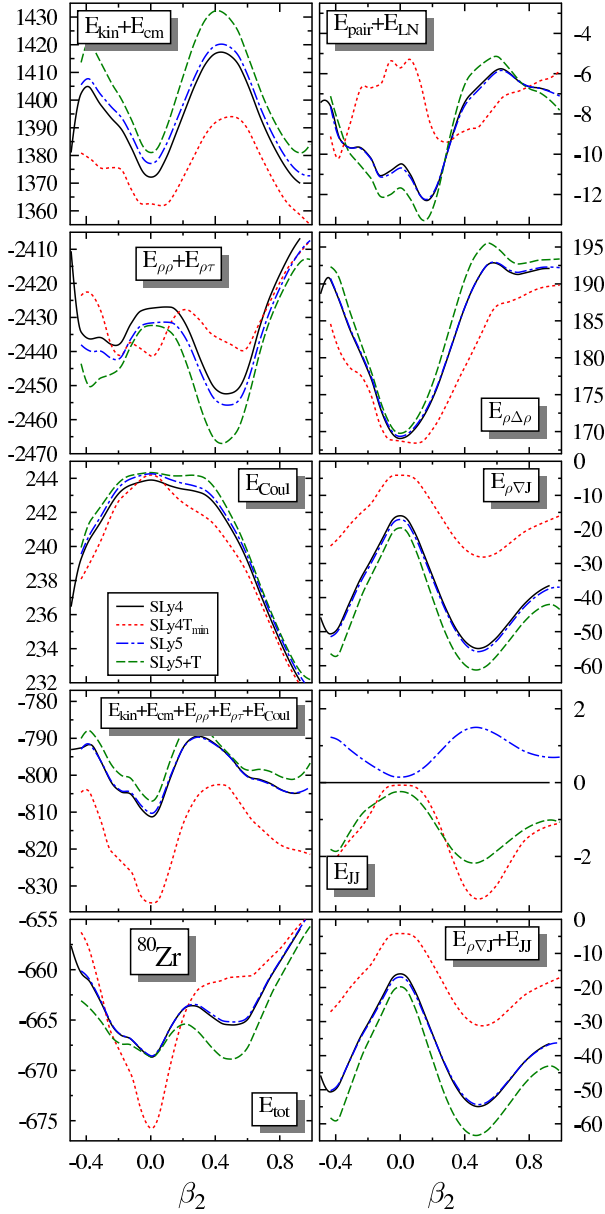


FIG. 24: (Color online) Same caption as Fig. 4, for  $^{80}\text{Zr}$ ,  $Z = N = 40$ .

has a dramatic effect on the energy curve, which shows a sharp spherical minimum. The large reduction of the spin-orbit strength is making this nucleus doubly-magic and pushes the deformed minimum to a very high energy, although the tensor interaction for SLy4T is more attractive for deformed configurations. This effect is corrected for by TZA. However, none of the parameterizations gives a deformed ground state, a deficiency shared by many modern Skyrme interactions [21].

The decomposition of the energy into its central and spin-orbit+tensor components is given in Fig. 23 for the interactions T22, T24 and T26, and Fig. 24 for SLy4, SLy4T<sub>min</sub>, SLy5 and SLy5+T. They confirm the result found for  $^{56}\text{Ni}$ , the topography of the energy curves re-

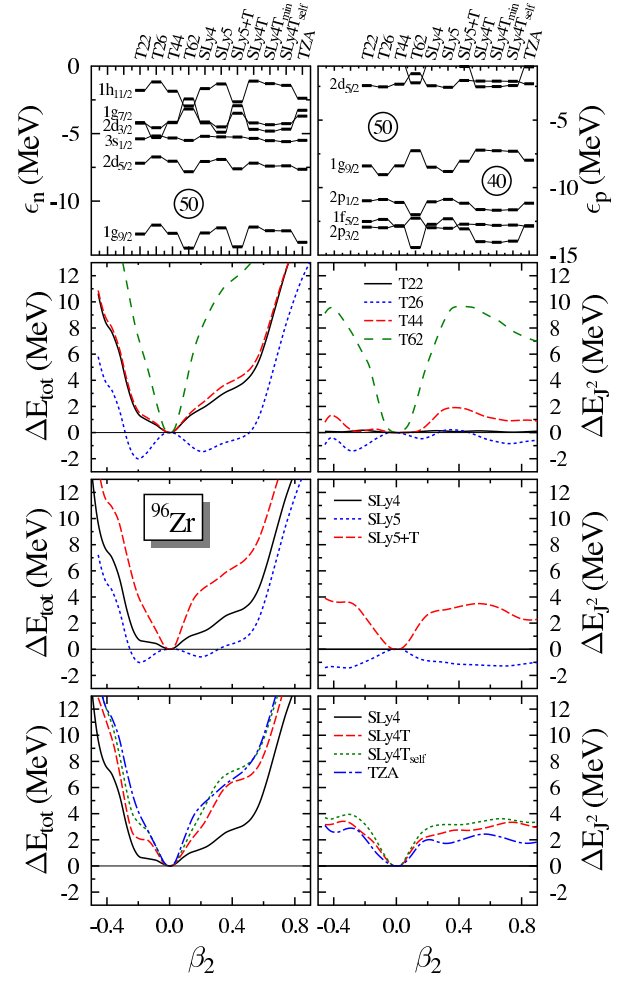


FIG. 25: (Color online) Same caption as Fig. 8, for  $^{96}\text{Zr}$ .

sult from subtle cancellations between the bulk contributions and the terms containing gradients. Again, the comparison of different parameterizations indicates that the readjustment of the parameters counteracts the self-consistency effects. The results obtained using variational interactions are qualitatively very similar. On the contrary, all components of the energy calculated with perturbative interactions are significantly different from those of the original interaction. A major qualitative difference with  $^{56}\text{Ni}$  is that the bulk terms give coexisting near-degenerate spherical and deformed minima in  $^{80}\text{Zr}$ , and that the compensation between the gradient, spin-orbit and tensor terms can tip the balance in one or the other direction. A weak spin-orbit strength, such as for the SLy4T interaction, now has the effect of favoring the spherical minimum much too strongly, pushing the deformed minimum very high in energy.

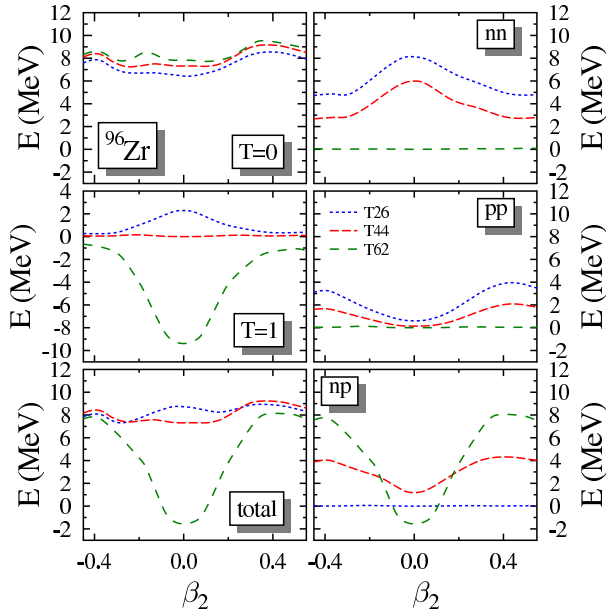


FIG. 26: (Color online) Same caption as Fig. 13, but for  $^{96}\text{Zr}$ .

### 3. $^{96}\text{Zr}$

The  $^{96}\text{Zr}$  isotope combines spherical sub-shell closures at  $N = 56$  and  $Z = 40$ . Its low-energy spectrum exhibits several unusual features. The systematics of masses in its immediate vicinity, a first  $2^+$  level with a large excitation energy and one of the smallest  $B(E2)$  values known in heavy nuclei are all consistent with the expectation that  $^{96}\text{Zr}$  is a rigid spherical nucleus. Other observables indicate the fragility of both shells. The  $B(E3)$  value of the  $3_1^- \rightarrow 0_1^+$  transition is among the strongest known for a vibrational nucleus [67, 68], the charge radius is enhanced compared to the droplet-model trend [69], thereby pointing to substantial ground-state correlations, and the  $g$  factors of the  $2_1^+$  and  $3_1^-$  hint at a complex superposition of several neutron and proton excitations across sub-shell closures [70]. It also shares with  $^{90}\text{Zr}$  and  $^{98}\text{Zr}$  the rare feature to have a low-lying  $0^+$  state as a first excited state [71]. As for many of the light doubly-magic nuclei studied above, this  $0^+$  state is interpreted as a deformed state resulting from the simultaneous 2p-2h excitation of protons and neutrons across the respective gaps [72].

The single-particle spectra at spherical shape and the energy curves of  $^{96}\text{Zr}$  are presented in Fig 25. As in  $^{90}\text{Zr}$ , the neutrons are spin-unsaturated and the protons spin-saturated. However, in this case, two levels contribute to the neutron spin-current density at sphericity,  $1g_{9/2+}$  and  $2d_{5/2+}$ ; hence, this density is larger than in  $^{90}\text{Zr}$ . Thanks to that, the differences between the interactions are amplified. In particular, the contribution from the isovector tensor terms might become very large as can be seen in Fig. 26, and drastically change the distance and even ordering of the single-particle levels; see Fig. 25. Compared to T22, T26 and T44, the parameterization

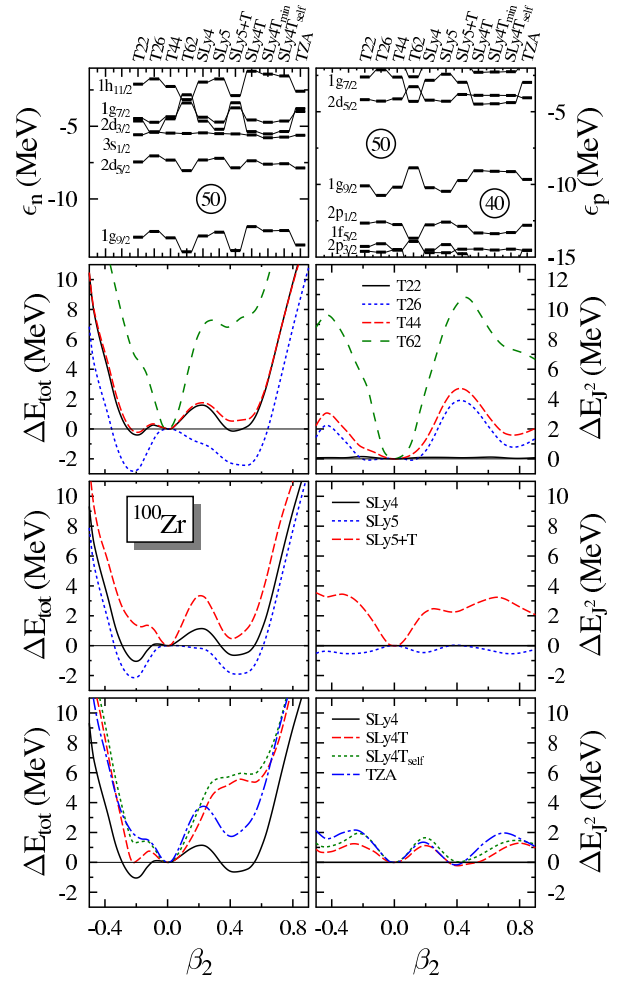


FIG. 27: (Color online) Same caption as Fig. 8, but for  $^{100}\text{Zr}$ ,  $Z = 40$ ,  $N = 60$ .

T62 gives much larger  $N = 56$  and  $Z = 40$  gaps, and also pushes up the  $2d_{3/2+}$  and  $1g_{7/2+}$  neutron levels, both located above the Fermi energy. The SLy5+T interaction has the same tendency, but in a less pronounced way. At least one of the tensor coupling constants is negative for both interactions.

The deformed minima obtained with the T26 and SLy5 interactions are at variance with data, as is the very stiff energy surface obtained with T62.

### 4. $^{100}\text{Zr}$

A large set of experimental data (charge radii [69], rotational bands [73] and  $B(E2)$  values [74]) demonstrate that  $^{100}\text{Zr}$  is located in a region of deformed nuclei. An excited band built on a  $0^+$  state coexisting with the ground-state band [73], and the large  $E0$  transition strength between the  $0^+$  states [75] indicate the coexistence of shapes with different deformations, the state with the largest deformation being the ground state.

The single-particle spectra at spherical shape, the deformation energy curve and the variation of the tensor energy are plotted against quadrupole deformation in Fig. 27. The overall behavior of the tensor energy shows many similarities with  $^{96}\text{Zr}$ . The results obtained with the T44 and T62 parameterizations indicate, however, a larger contribution from the isovector tensor terms. The four additional neutrons shift the neutron Fermi energy into a region of large level density above the  $N = 56$  sub-shell closure. The positions of the  $2d_{3/2+}$  and  $2g_{7/2+}$  are very much dependent on the sign and size of the isovector coupling constant  $C_1^J$ . For a positive value as in T26, the  $2d_{3/2+}$  level is close to the Fermi level and is occupied in such a way that it partially cancels the contribution from the  $2d_{5/2+}$  orbital. The isovector tensor terms are in this case strongly reduced. In contrast, for a negative  $C_1^J$  coefficient as in T62, the  $2d_{3/2+}$  level is pushed up and crosses the  $1h_{11/2-}$  level, increasing the neutron spin-current density. Results obtained with the SLy5+T interaction, for which  $C_1^J$  is also negative, are similar, although less pronounced. For even larger negative values of the tensor coupling constants, this feedback mechanism will ultimately generate an abnormal level ordering for certain mid-shell nuclei, cf. the appendix B of Article I. For SLy4T and SLy4T<sub>self</sub>, this feedback mechanism is suppressed by the reduced spin-orbit interaction, whereas for TZa, it is present.

Most total deformation energy curves in Fig. 27 exhibit spherical, prolate and oblate minima. The inclusion of beyond mean-field correlations should favor the prolate minima and create a  $0^+$  excitation exhibiting some amount of configuration mixing. Such results are consistent with experiment. The spherical minimum is too much below the deformed one to expect that additional correlations from the projection of  $J = 0$  states will make  $^{100}\text{Zr}$  deformed in its ground state. For T62, the deformation energy curve looks like that of a doubly-magic nucleus. For SLy4T and SLy4T<sub>self</sub>, it is the reduced spin-orbit interaction that reinforces the proton  $Z = 40$  shell closure. The prolate minimum becomes a shoulder around 5 MeV, leading to the coexistence of spherical and oblate minima.

### 5. $^{110}\text{Zr}$

The only experimental information available about the very neutron-rich  $^{110}\text{Zr}$  is that it is a bound nucleus [76]. It presents the particularity to combine two spin-saturated oscillator shells,  $Z = 40$  and  $N = 70$ . The corresponding gaps are still large for parameterizations like SLy4T and SLy4T<sub>self</sub> with a reduced spin-orbit strength and  $^{110}\text{Zr}$  behaves like a doubly-magic nucleus. For all other parameterizations, but T62, weak sub-shell closures remain at both these nucleon numbers. The gaps are too small to enforce a rigid spherical shape, but sufficient to prevent the existence of a clear-cut unique deformed minimum to describe the ground-state. Instead,

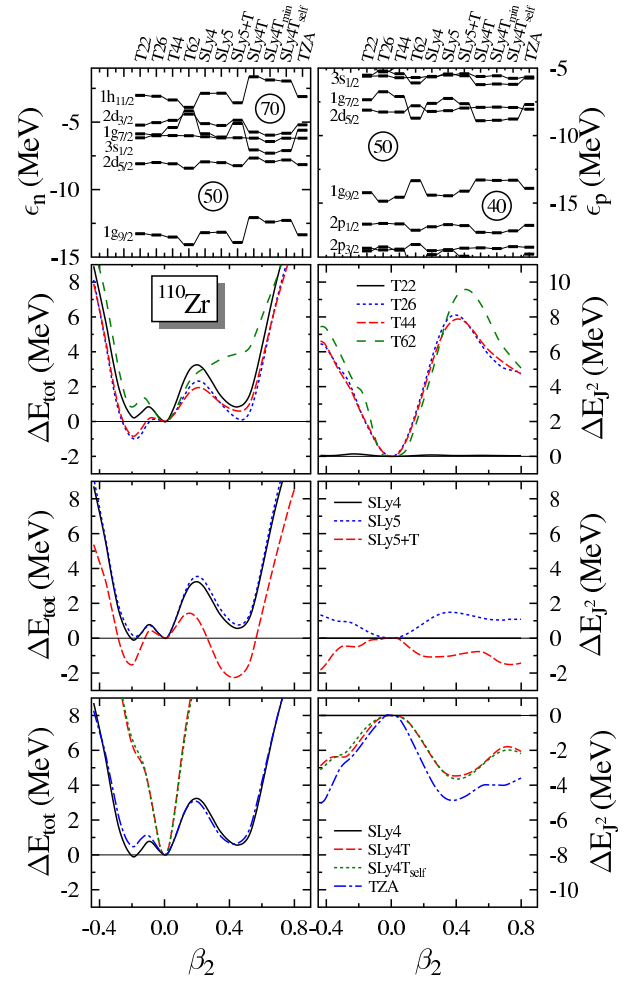


FIG. 28: (Color online) Same caption as Fig. 8, for  $^{110}\text{Zr}$ ,  $Z = 40$ ,  $N = 70$ .

all interactions, but SLy4T, SLy4T<sub>self</sub> and T62, predict a complicated pattern of three coexisting spherical, prolate and oblate structures. For T62, there is no prolate minimum, and the spherical configuration is favored because of the semi-magic character of this nucleus with a large  $Z = 40$  shell closure. For SLy4T and SLy4T<sub>self</sub>, there is a single, very sharp spherical minimum typical of a doubly-magic character.

## F. Heavy semi-magic nuclei

Let us conclude our survey with two selected heavy semi-magic nuclei.

### 1. $^{120}\text{Sn}$

The stable semi-magic  $^{120}\text{Sn}$  is the lightest of heavy tin isotopes for which no coexisting deformed rotational band at low excitation energy has been observed [77].

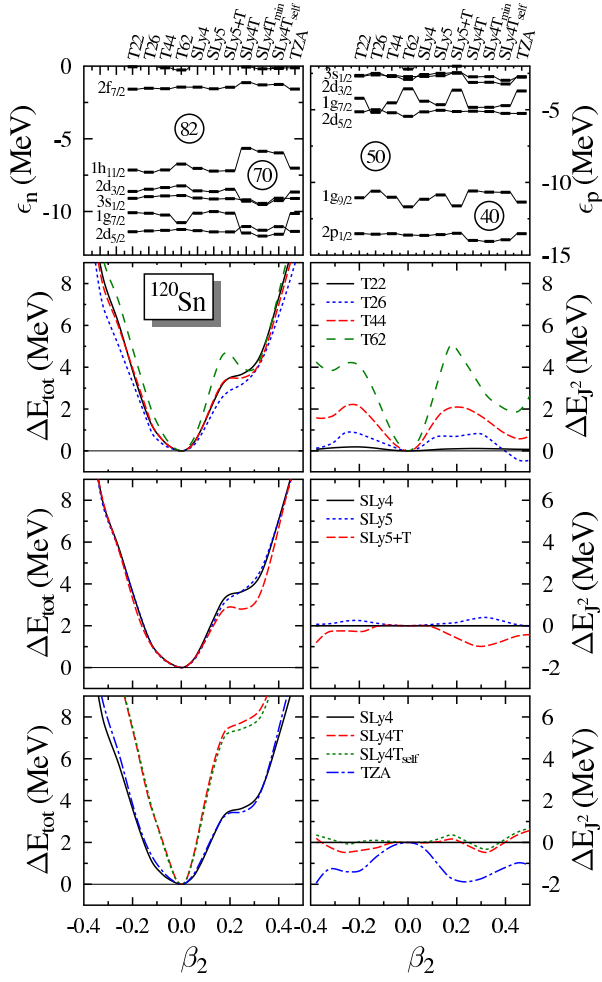


FIG. 29: (Color online) Same caption as Fig. 8, for  $^{120}\text{Sn}$ ,  $Z = 50$ ,  $N = 70$ . All panels share the same energy scale.

The neutron number  $N = 70$  of  $^{120}\text{Sn}$  corresponds to a magic number for neutrons in a pure harmonic oscillator picture. This simple picture is destroyed by the spin-orbit interaction which pushes the  $1h_{11/2-}$  across the  $N = 70$  gap, creating a shell closure at  $N = 82$ . In fact, data suggest that this oscillator shell does not survive even as a subshell closure, as the empirical  $11/2^-$  intruder level is below the  $3/2^+$  level and degenerate with the  $1/2^+$  state in  $^{132}\text{Sn}$ . As already mentioned above, it is a well-known problem of virtually all energy functionals that the  $1h_{11/2-}$  intruder level is predicted to lie slightly above the  $gds$  shell [2]. This deficiency was related in Fig. 17 of Article I to a too high position of the centroid of the  $1h$  levels.

The energy surfaces obtained with the  $TIJ$  interactions are presented on the left-hand side of Fig. 29, the Nilsson diagrams for four selected parameterizations in Fig. 30. The neutron contribution to the tensor energy is small at sphericity, as the neutrons are predicted to be spin saturated, see Fig. 30, at variance with experiment. As soon as deformation sets in, the tensor energy

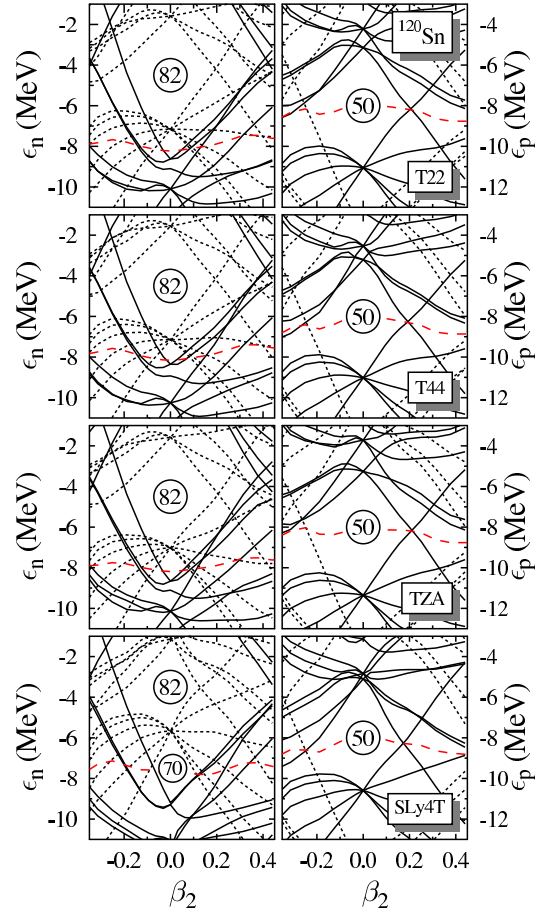


FIG. 30: (Color online) Proton and neutron Nilsson diagrams for  $^{120}\text{Sn}$  obtained with the parameterizations as indicated. Solid lines denote levels of positive parity, dotted lines levels of negative parity, and the red dashed lines denote the Fermi energy.

increases for the four  $TIJ$  parameterizations. However, the total energy curves are much closer than one would expect from the difference between the tensor energies. The most significant difference is obtained for deformations between the spherical minimum and the prolate shoulder.

The energy curves calculated with the SLy4, SLy5 and SLy5+T interactions are nearly identical, except for a small lowering of the prolate shoulder for the latter.

The situation is quite different for SLy4T. As a consequence of its weak spin-orbit strength, the neutron intruder level is halfway in the gap between the major shells. The energy gap at  $N = 70$  remains very large and significantly reduces the neutron level density around the Fermi energy for deformations up to  $\beta_2$  values around 0.1. The tensor energy decreases with deformation, but not sufficiently to compensate the effect of the decrease of the spin-orbit strength. The net effect on the energy curve is that it is much stiffer than with the original SLy4 parameters, artificially making  $^{120}\text{Sn}$  a doubly-magic nucleus similar to  $^{132}\text{Sn}$ .

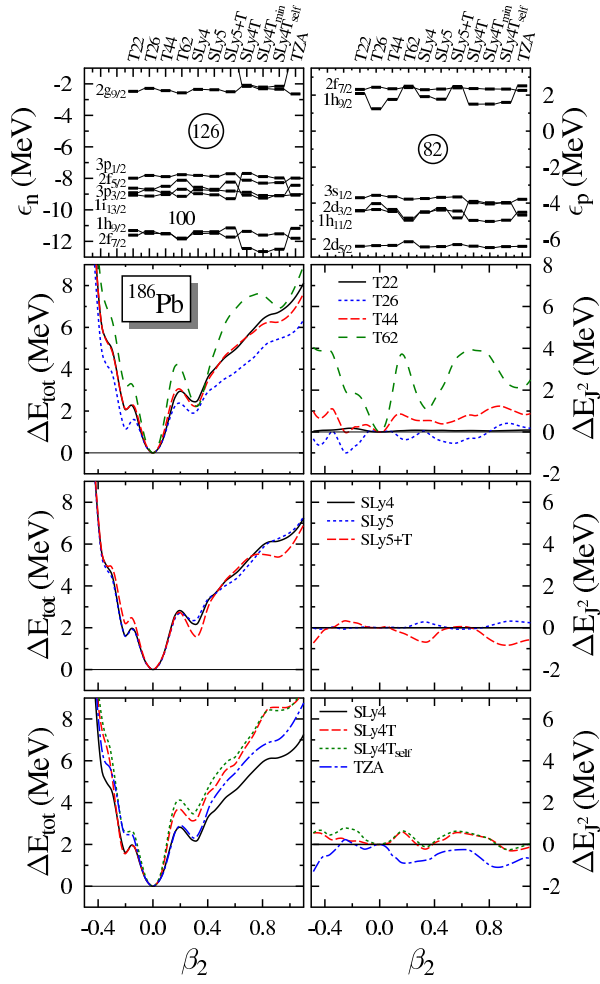


FIG. 31: (Color online) Same caption as Fig. 10, but for  $^{186}\text{Pb}$ ,  $Z = 82$ ,  $N = 104$ .

## 2. $^{186}\text{Pb}$

The heavy, neutron-deficient  $N = 104$ ,  $Z = 82$  Pb isotope,  $^{186}\text{Pb}$ , exhibits a triple shape coexistence of spherical, prolate and oblate shapes, with the unique feature that its two lowest excited levels are  $0^+$  states [78, 79]. The deformation energy curves obtained with all interactions tested here are plotted in Fig. 31. They are compatible with the experimental data and present a spherical minimum, and excited oblate, prolate, and often also superdeformed minima, in most cases all separated by small barriers.

The tensor energy and the impact of the tensor terms on the total energy are similar to those found for  $^{120}\text{Sn}$ . The differences between the  $TIJ$  interactions are the largest between the minima or shoulders; SLy5+T slightly moves the excitation energies of excited minima compared to SLy5, and the deformation energy curves from SLy4T and SLy4T<sub>self</sub> are stiffer than the others, at least for prolate deformations. The reduced spin-orbit strength for SLy4T and SLy4T<sub>self</sub> pulls the neutron

$1i_{13/2}^+$  intruder back towards the  $N = 126$  gap. This is inconsistent with the existence of a very low-lying isomeric  $13/2^+$  states located at a few tens of keV excitation energy in surrounding odd- $A$  Pb isotopes.  $\alpha$ -decay hindrance factors suggest indeed that this state is well described by a neutron in the  $1i_{13/2}^+$  level coupled to a spherical core [80].

Nuclei in this mass region are less affected by the tensor terms, as hinted already in Article I by the analysis of the spin-current density at spherical shape in the Pb isotopic chain. Still, the tensor terms modify the balance between the excitation energy of the coexisting minima. As the relative position of the minima is sensitive to all terms of the EDF, this quantity cannot be used to safely validate the tensor coupling constants.

## V. SUMMARY AND CONCLUSIONS

We have studied the impact of tensor terms in the Skyrme energy density functional on deformation properties of magic and semi-magic nuclei. This work is a continuation of a previous study limited to spherical symmetry, as published in Article I [6]. The study has been focussed on a representative sample of parameterizations introduced in Article I, which covers a wide range of values for the isoscalar and isovector tensor coupling constants and allow to disentangle their respective role. These parameterizations are adjusted with a fit protocol very similar to that of the successful SLy $x$  parameterizations [13, 14]. We also considered two other recent families of energy functionals also based on the SLy $x$  ones, but constructed following very different strategies. For the parameterization SLy5+T [5] a tensor force was perturbatively added to SLy5 without any readjustment of the other parameters. For SLy4T [8], the tensor and spin-orbit coupling constants were fixed without any readjustment of the other parameters of SLy4. The related parameterizations SLy4T<sub>min</sub> [8] and SLy4T<sub>self</sub> and TZA introduced here allow to disentangle the origin of the different results obtained with SLy4T and the  $TIJ$ s as being due to the perturbative fit, the change in the spin-orbit strength, or the choice of tensor coupling constants.

A first result that we have obtained concerns the order of magnitude of the different components of the tensor term. In spherical coordinates, it can be decomposed in vector and pseudotensor contributions. For all studied parameterizations for which the coefficients of both terms have the same order of magnitude, the pseudotensor contribution is at least one order of magnitude lower than the vector one. This justifies the common practice of neglecting the pseudovector contribution to the energy.

The shell effects induced by the tensor interaction fluctuate as a function of the filling of single-particle orbits. This effect has motivated the introduction of the tensor force to explain the evolution of the shell structure of spherical nuclei along isotopic lines. Inevitably, it leads also to a pattern for the size and deformation dependence



of the contribution of the tensor terms to the total energy which depends on the fillings of orbitals:

- (i) For doubly spin-saturated nuclei at sphericity, such as  $^{40}\text{Ca}$  and  $^{80}\text{Zr}$ , the tensor energy is close to zero at spherical shape, and increases in absolute value with deformation.
- (ii) For doubly spin-unsaturated doubly-magic nuclei such as  $^{56}\text{Ni}$ ,  $^{78}\text{Ni}$ ,  $^{100}\text{Sn}$ ,  $^{132}\text{Sn}$  and  $^{208}\text{Pb}$ , the absolute value of the tensor energy is the largest at sphericity, and decreases with deformation.
- (iii) For doubly spin-unsaturated doubly-magic  $N = Z$  nuclei like  $^{56}\text{Ni}$  and  $^{100}\text{Sn}$ , the tensor energy is obviously dominated by the isoscalar part of the tensor interaction. The same conclusion holds, however, also for the  $N \neq Z$  nuclei  $^{78}\text{Ni}$ ,  $^{132}\text{Sn}$  and  $^{208}\text{Pb}$ , in spite of their large asymmetry  $N - Z$ . The reason for that is that the proton and neutron spin-currents densities are very similar in size, sign and spatial distribution in these nuclei; hence, they nearly cancel each others' contribution to the isovector spin-current at all deformations.
- (iv) The isovector tensor contribution to the energy plays a significant role only for doubly-magic nuclei that combine a spin-saturated configuration for one nucleon species with a spin-unsaturated configuration for the other, such as in  $^{48}\text{Ca}$ ,  $^{68}\text{Ni}$ , and  $^{90}\text{Zr}$ .
- (v) The behavior of nuclei without large shell or sub-shell closures for at least one nucleon species does not follow simple rules. These nuclei are most sensitive to the values of the tensor coupling constants, at least within the sample of nuclei studied here. In nuclei with a large density of single-particle levels around the Fermi surface, there are highly nonlinear feedback effects at play. For large absolute values of their coupling constants, the tensor terms reduce or amplify themselves through the reordering of levels around the Fermi energy, as exemplified by  $^{96}\text{Zr}$  and  $^{100}\text{Zr}$ .

Self-consistency is implemented at two different levels in the method that we have used: in the fitting procedure of the interaction and in the solution of the mean-field equations.

- (i) The perturbative addition of only a tensor term, like for SLy5+T, to an existing parameterization will modify all contributions to the mean fields and the energy.
- (ii) The self-consistency of the mean-field induces a rearrangement of the single-particle wave functions, and consequently of all densities affecting at the end all observables. This effect is exemplified by the comparison between the results obtained with SLy5 and SLy5+T, which share all coupling constants except those of the tensor terms.

- (iii) Using a protocol mainly based on infinite nuclear matter properties, binding energies and charge radii, as the Saclay-Lyon protocol [13, 14], the changes in the coupling constants due to the self-consistency of fits tend to counteract the self-consistency in the mean field. This is exemplified by the comparison between the results obtained with SLy4, SLy5 and SLy5+T. For most nuclei studied here and for most quantities not directly affected by the tensor terms, the differences between the predictions of the first two are on a much smaller scale than the differences between the latter two. A perturbative modification of a well-adjusted parameterization might spoil its predictive power in unexpected ways. Our results confirm the suspicion of the authors of the perturbatively constructed SLy5+T [5], who indeed intended their interaction as a tool for explorative studies only, and state that "an ambitious refitting program [...] should be [...] undertaken" for more detailed studies.
- (iv) Self-consistency of the fits and/or the calculations has the consequence that the total deformation energy obtained with different interactions varies in most cases on a much smaller scale than the tensor contributions. In some cases such as  $^{80}\text{Zr}$ , they even might go into opposite directions.
- (v) The tensor and spin-orbit contributions to the total energy and to the spin-orbit fields are tightly interwoven. Constraining both too tightly in a small region of the nuclear chart might be misleading when aiming at a universal functional. This is exemplified by SLy4T with its spin-orbit and tensor coupling constants fitted very carefully to suitably chosen spin-orbit splittings in  $^{40}\text{Ca}$ ,  $^{48}\text{Ca}$  and  $^{56}\text{Ni}$ . The failure of SLy4T to extrapolate well clearly points to missing physics, either in the form of missing terms in the functional or missing correlations.
- (vi) The strong reduction of the spin-orbit strength for SLy4T improves the description of spin-orbit splittings in light nuclei, but amplifies the problems from the wrong positioning of centroids. Also, the spin-orbit splittings in heavy nuclei are much too small. The strong reduction of the spin-orbit strength to about 2/3 its original value is specific to the SLy4-based interaction constructed in [8]. For their SkP and SkO based fits, the reduction is much more moderate.

The size and deformation dependence of the tensor energy is correlated with the impact of the tensor terms on single-particle spectra. In Article I, we analyzed how the tensor terms affect the position and relative distance of single-particle energies for spherical shapes. Concerning the dependence of Nilsson diagrams on the tensor force, the following can be stated:

- (i) Tensor terms modify the slope of the levels in the Nilsson diagram. For the magic nuclei studied here

this happens in particular around sphericity, where the tensor contribution to the spin-orbit field  $W_{q,\mu\nu}$  often changes rapidly with deformation.

- (ii) When comparing interactions with different values of the tensor coupling constants that are otherwise completely refitted, the change in slope compensates at large deformations to a large extent the differences between single-particle spectra found at spherical shape. For those interactions, the deformed single-particle spectra around the Fermi energy are often nearly identical in spite of the different tensor interactions. In such fit protocol, the coupling constants of the tensor terms control the balance between spherical and deformed shell gaps.
- (iii) In perturbative fits, in particular those where more than one term is rescaled, deformed shell structure is affected as well.

It can be expected that these findings are to a large extent independent of remaining deficiencies of the central and spin-orbit interactions, and will be of great value for the construction of future, improved energy function-

als. We will address the question of how the surface and surface symmetry energy coefficients of the interactions change as a function of the coupling constants of the tensor terms, and how this correlates with energy at large deformation in future work. A study of the so-called "time-odd terms" in the energy functional that originate from a tensor force is underway as well. A point of special interest will be the analysis of potential finite-size instabilities using the technique of Ref. [81, 82].

### Acknowledgments

This work was supported by the "Interuniversity Attraction Pole" (IUAP) of the Belgian Scientific Policy Office under project P6/23; by the U.S. National Science Foundation under Grant NoPHY-0456903, and by the U.S. Department of Energy under Contract Nos. DE-FG02-96ER40963, DE-FG02-07ER41529 (University of Tennessee) and DE-AC05-00OR22725 with UT-Battelle, LLC (Oak Ridge National Laboratory).

- 
- [1] T. Otsuka, T. Suzuki, R. Fujimoto, H. Grawe, and Y. Akaishi, *Phys. Rev. Lett.* **95**, 232502 (2005).
  - [2] M. Bender, P.-H. Heenen, and P.-G. Reinhard, *Rev. Mod. Phys.* **75**, 121 (2003).
  - [3] T. Otsuka, T. Matsuo, and D. Abe, *Phys. Rev. Lett.* **97**, 162501 (2006).
  - [4] B. A. Brown, T. Duguet, T. Otsuka, D. Abe, and T. Suzuki, *Phys. Rev. C* **74**, 061303(R) (2006).
  - [5] G. Colò, H. Sagawa, S. Fracasso, and P. F. Bortignon, *Phys. Lett. B* **646**, 227 (2007), Erratum *Phys. Lett. B* **668**, 457 (2008).
  - [6] T. Lesinski, M. Bender, K. Bennaceur, T. Duguet, and J. Meyer, *Phys. Rev. C* **76**, 014312 (2007).
  - [7] W. Zou, G. Colò, Z. Ma, H. Sagawa, and P. F. Bortignon, *Phys. Rev. C* **77**, 014314 (2008).
  - [8] M. Zalewski, J. Dobaczewski, W. Satuła, and T. R. Werner, *Phys. Rev. C* **77**, 024316 (2008).
  - [9] T. Duguet and T. Lesinski, *Eur. Phys. J. Special Topics* **156**, 207 (2008).
  - [10] M. Bender, G. F. Bertsch, and P.-H. Heenen, *Phys. Rev. C* **73**, 034322 (2006).
  - [11] M. Bender, G. F. Bertsch, and P.-H. Heenen, *Phys. Rev. C* **78**, 054312 (2008).
  - [12] M. Kortelainen, J. Dobaczewski, K. Mizuyama, and J. Toivanen, *Phys. Rev. C* **77**, 064307 (2008).
  - [13] E. Chabanat, P. Bonche, P. Haensel, J. Meyer, and R. Schaeffer, *Nucl. Phys. A* **627**, 710 (1997).
  - [14] E. Chabanat, P. Bonche, P. Haensel, J. Meyer, and R. Schaeffer, *Nucl. Phys. A* **635**, 231 (1998), *ibid.* **643**, 441(E) (1998).
  - [15] E. Perlińska, S. G. Rohoziński, J. Dobaczewski, and W. Nazarewicz, *Phys. Rev. C* **69**, 014316 (2004).
  - [16] D. Vautherin and D. M. Brink, *Phys. Rev. C* **5**, 626 (1972).
  - [17] P. Bonche, H. Flocard, and P.-H. Heenen, *Nucl. Phys. A* **467**, 115 (1987).
  - [18] J. Dobaczewski, J. Dudek, S. G. Rohoziński, and T. R. Werner, *Phys. Rev. C* **62**, 014310 (2000).
  - [19] T. H. R. Skyrme, *Phil. Mag.* **1**, 1043 (1956).
  - [20] T. H. R. Skyrme, *Nucl. Phys.* **9**, 615 (1958).
  - [21] P.-G. Reinhard, D. J. Dean, W. Nazarewicz, J. Dobaczewski, J. A. Maruhn, and M. R. Strayer, *Phys. Rev. C* **60**, 014316 (1999).
  - [22] N. Chamel, S. Goriely, and J. M. Pearson, *Nucl. Phys. A* **812**, 72 (2008).
  - [23] M. V. Stoitsov, J. Dobaczewski, W. Nazarewicz, and P. Ring, *Comput. Phys. Comm.* **167**, 43 (2005).
  - [24] S. Åberg, H. Flocard, and W. Nazarewicz, *Annu. Rev. Part. Sci.* **40**, 439 (1990).
  - [25] C. L. Bai, H. Sagawa, H. Q. Zhang, X. Z. Zhang, G. Colò, and F. R. Xu, *Phys. Lett. B* **28**, 675 (2009).
  - [26] C. L. Bai, H. Q. Zhang, X. Z. Zhang, F. R. Xu, H. Sagawa, and G. Colò, *Phys. Rev. C* **79**, 041301(R) (2009).
  - [27] See EPAPS document No. XXXXXXXX for the coupling constants of the SLy4T<sub>self</sub> and TZA parametrizations. For more information on EPAPS, see <http://www.aip.org/pubservs/epaps.html>.
  - [28] P. Bonche, H. Flocard, P.-H. Heenen, S. J. Krieger, and M. S. Weiss, *Nucl. Phys. A* **443**, 39 (1985).
  - [29] P. Bonche, H. Flocard, and P.-H. Heenen, *Comput. Phys. Comm.* **171**, 49 (2005).
  - [30] C. Rigollet, P. Bonche, H. Flocard, and P.-H. Heenen, *Phys. Rev. C* **59**, 3120 (1999).
  - [31] M. Bender, H. Flocard, and P. H. Heenen, *Phys. Rev. C* **68**, 044321 (2003).
  - [32] M. Bender, P. Bonche, T. Duguet, and P.-H. Heenen, *Phys. Rev. C* **69**, 064303 (2004).

- [33] M. Bender and P.-H. Heenen (2009), unpublished.
- [34] J. S. Berryman, K. Minamisono, W. F. Rogers, B. A. Brown, H. L. Crawford, G. F. Grinyer, P. F. Mantica, J. B. Stoker, and I. S. Towner, *Phys. Rev. C* **79**, 064305 (2009).
- [35] J. N. Orce, B. Crider, S. Mukhopadhyay, E. Peters, E. Elhami, M. Scheck, B. Singh, M. T. McEllistrem, and S. W. Yates, *Phys. Rev. C* **77**, 064301 (2008).
- [36] T. Otsuka, M. Honma, and T. Mizusaki, *Phys. Rev. Lett.* **81**, 1588 (1998).
- [37] L. Trache, A. Kolomiets, S. Shlomo, K. Heyde, H. Dejbakhsh, C. A. Gagliardi, R. E. Tribble, X. G. Zhou, V. E. Jacob, and A. M. Oros, *Phys. Rev. C* **54**, 2361 (1996).
- [38] D. Rudolph, C. Baktash, M. J. Brinkman, E. Caurier, D. J. Dean, M. Devlin, J. Dobaczewski, P.-H. Heenen, H.-Q. Jin, D. R. LaFosse, W. Nazarewicz, F. Nowacki, A. Poves, L. L. Riedinger, D. G. Sarantites, W. Satuła, and C.-H. Yu, *Phys. Rev. Lett.* **82**, 3763 (1999).
- [39] R. R. Chasman, *Phys. Rev. Lett.* **99**, 082501 (2007).
- [40] M. Bender, P. Bonche, and P.-H. Heenen, *Phys. Rev. C* **74**, 024312 (2006).
- [41] E. Ideguchi, D. G. Sarantites, W. Reviol, A. V. Afanasjev, M. Devlin, C. Baktash, R. V. F. Janssens, D. Rudolph, A. Axelsson, M. P. Carpenter, A. Galindo-Uribarri, D. R. LaFosse, T. Lauritsen, F. Lerma, C. J. Lister, P. Reiter, D. Seweryniak, M. Weiszflog, and J. N. Wilson, *Phys. Rev. Lett.* **87**, 222501 (2001).
- [42] C. J. Chiara, E. Ideguchi, M. Devlin, D. R. LaFosse, F. Lerma, W. Reviol, S. K. Ryu, D. G. Sarantites, C. Baktash, A. Galindo-Uribarri, M. P. Carpenter, R. V. F. Janssens, T. Lauritsen, C. J. Lister, P. Reiter, D. Seweryniak, P. Fallon, A. Görgen, A. O. Macchiavelli and D. Rudolph, *Phys. Rev. C* **67**, 041303(R) (2003).
- [43] R. Broda, B. Fornal, W. Królas, T. Pawlat, D. Bazzacco, S. Lunardi, C. Rossi-Alvarez, R. Menegazzo, G. de Angelis, P. Bednarczyk, J. Rico, D. De Acuña, P. J. Daly, R. H. Mayer, M. Sferrazza, H. Grawe, K. H. Maier, and R. Schubart, *Phys. Rev. Lett.* **74**, 868 (1995).
- [44] T. Ishii, M. Asai, A. Makishima, I. Hossain, M. Ogawa, J. Hasegawa, M. Matsuda, and S. Ichikawa, *Phys. Rev. Lett.* **84**, 39 (2000).
- [45] O. Sorlin, S. Leenhardt, C. Donzau, J. Duprat, F. Azaiez, F. Nowacki, H. Grawe, Z. Dombrádi, F. Amorini, A. Astier, D. Baiborodin, M. Belleguic, C. Borcea, C. Bourgeois, D. M. Cullen, Z. Dlouhy, E. Dragulescu, M. Górski, S. Grévy, D. Guillemaud-Mueller, G. Hagemann, B. Herskind, J. Kiener, R. Lemmon, M. Lewitowicz, S. M. Lukyanov, P. Mayet, F. de Oliveira Santos, D. Pantalica, Yu.-E. Penionzhkevich, F. Pougheon, A. Poves, N. Redon, M. G. Saint-Laurent, J. A. Scarpaci, G. Sletten, M. Stanoiu, O. Tarasov, and Ch. Theisen, *Phys. Rev. Lett.* **88**, 092501 (2002).
- [46] N. Bree, I. Stefanescu, P. A. Butler, J. Cederkäll, T. Davinson, P. Delahaye, J. Eberth, D. Fedorov, V. N. Fedosseev, L. M. Fraile, S. Franchoo, G. Georgiev, K. Gladniskhi, M. Huyse, O. Ivanov, J. Iwanicki, J. Jolie, U. Köster, Th. Kröll, R. Krücken, B. A. Marsh, O. Niedermaier, P. Reiter, H. Scheit, D. Schwalm, T. Sieber, J. Van de Walle, P. Van Duppen, N. Warr, D. Weisshaar, F. Wenander, and S. Zemlyanov, *Phys. Rev. C* **78**, 047301 (2008).
- [47] S. Rahaman, J. Hakala, V. Elomaa, T. Eronen, U. Hager, A. Jokinen, A. Kankainen, I. Moore, H. Penttilä, S. Rinta-Antila, J. Rissanen, A. Saastamoinen, C. Weber, and J. Äystö, *Eur. Phys. J. A* **34**, 5 (2007).
- [48] C. Guénaut, G. Audi, D. Beck, K. Blaum, G. Bollen, P. Delahaye, F. Herfurth, A. Kellerbauer, H.-J. Kluge, J. Libert, D. Lunney, S. Schwarz, L. Schweikhard, and C. Yazidjian, *Phys. Rev. C* **75**, 044303 (2007).
- [49] H. Grawe, M. Górski, J. Döring, C. Fahlander, M. Palacz, F. Nowacki, E. Caurier, J. M. Daugas, M. Lewitowicz, M. Sawicka, M. Pfützner, R. Grzywacz, K. Rykaczewski, O. Sorlin, S. Leenhardt, F. Azaiez, M. Rejmund, K. Hauschild and J. Uusitalo, in *Tours Symposium on Nuclear Physics IV*, edited by M. Lewitowicz, Y. T. Oganessian, H. Akimune, M. Ohta, H. Utsunomiya, T. Yamagata, M. Arnould, and T. Wada (AIP, 2001), vol. 561 of *AIP Conf. Proc.*, pp. 287–300.
- [50] H. Grawe and M. Lewitowicz, *Nucl. Phys. A* **693**, 116 (2001).
- [51] K. Langanke, J. Terasaki, F. Nowacki, D. J. Dean, and W. Nazarewicz, *Phys. Rev. C* **67**, 044314 (2003).
- [52] T. Kibédi and R. H. Spear, *Atom. Data Nucl. Data Tables* **89**, 77 (2005).
- [53] C. Engelmann, F. Ameil, P. Armbruster, M. Bernas, S. Czajkowski, P. Dessagne, C. Donzau, H. Geissel, A. Heinz, Z. Janas, C. Kozhuharov, Ch. Miehe, G. Münzenberg, M. Pfützner, C. Röhl, A. Schwab, C. Stéphan, K. Sümmerer, L. Tassan-Got, and B. Voss, *Z. Phys. A* **352**, 351 (1995).
- [54] P. T. Hosmer, H. Schatz, A. Aprahamian, O. Arndt, R. R. C. Clement, A. Estrade, K.-L. Kratz, S. N. Liddick, P. F. Mantica, W. F. Mueller, F. Montes, A. C. Morton, M. Ouellette, E. Pellegrini, B. Pfeiffer, P. Reeder, P. Santi, M. Steiner, A. Stolz, B. E. Tomlin, W. B. Walters, and A. Wöhr, *Phys. Rev. Lett.* **94**, 112501 (2005).
- [55] J. Hakala, S. Rahaman, V.-V. Elomaa, T. Eronen, U. Hager, A. Jokinen, A. Kankainen, I. D. Moore, H. Penttilä, S. Rinta-Antila, J. Rissanen, A. Saastamoinen, T. Sonoda, C. Weber, and J. Äystö, *Phys. Rev. Lett.* **101**, 052502 (2008).
- [56] R. Schneider, J. Friese, J. Reinhold, K. Zeitelhack, T. Faestermann, R. Gernhäuser, H. Gilg, F. Heine, J. Homolka, P. Kienle, H. J. Körner, H. Geissel, G. Münzenberg, and K. Sümmerer, *Z. Phys A* **348**, 241 (1994).
- [57] M. Lewitowicz, R. Anne, G. Auger, D. Bazin, C. Borcea, V. Borrel, J. M. Corre, T. Dörfler, A. Fomichev, R. Grzywacz, D. Guillemaud-Mueller, R. Hue, M. Huyse, Z. Janas, H. Keller, S. Lukyanov, A. C. Mueller, Yu. Penionzhkevich, M. Pfützner, F. Pougheon, K. Rykaczewski, M. G. Saint-Laurent, K. Schmidt, W. D. Schmidt-Ott, O. Sorlin, J. Szerypo, O. Tarasov, J. Wauters and J. Zylicz, *Phys. Lett. B* **332**, 20 (1994).
- [58] D. Seweryniak, M. P. Carpenter, S. Gros, A. A. Hecht, N. Hoteling, R. V. F. Janssens, T. L. Khoo, T. Lauritsen, C. J. Lister, G. Lotay, D. Peterson, A. P. Robinson, W. B. Walters, X. Wang, P. J. Woods, and S. Zhu, *Phys. Rev. Lett.* **99**, 022504 (2007).
- [59] J. Eberth, R. A. Meyer, and K. Sistemich, eds., *Proceedings of the International Workshop on Nuclear Structure of the Zirconium Region, Bad Honnef, 1988* (Springer, Berlin and Heidelberg, 1988).
- [60] F. Tondeur, *Nucl. Phys. A* **359**, 278 (1981).
- [61] J. Skalski, P. H. Heenen, and P. Bonche, *Nucl. Phys. A* **559**, 221 (1993).
- [62] C. J. Lister, M. Campbell, A. A. Chishti, W. Gelletly, L. Goettig, R. Moscrop, B. J. Varley, A. N. James, T.

- Morrison, H. G. Price, J. Simpson, K. Connel, and O. Skeppstedt, *Phys. Rev. Lett.* **59**, 1270 (1987).
- [63] C. J. Lister, P. J. Ennis, A. A. Chishti, B. J. Varley, W. Gelletly, H. G. Price, and A. N. James, *Phys. Rev. C* **42**, R1191 (1990).
- [64] S. M. Fischer, C. J. Lister, D. P. Balamuth, R. Bauer, J. A. Becker, L. A. Bernstein, M. P. Carpenter, J. Durell, N. Fotiades, S. J. Freeman, P. E. Garrett, P. A. Hausladen, R. V. F. Janssens, D. Jenkins, M. Leddy, J. Ressler, J. Schwartz, D. Svelnys, D. G. Sarantites, D. Seweryniak, B. J. Varley, R. Wyss, *Phys. Rev. Lett.* **87**, 132501 (2001).
- [65] S. D. Paul, C. Baktash, W. Satula, C. J. Gross, I. Birieli, R. M. Clark, R. A. Cunningham, M. Devlin, P. Fallon, A. Galindo-Uribarri, T. Ginter, D. R. Lafosse, J. Kay, F. Lerma, I. Y. Lee, C. Leyland, A. O. Macchiavelli, B. D. MacDonald, S. J. Metcalfe, A. Piechaczek, D. C. Radford, W. Reviol, L. L. Riedinger, D. Rudolph, K. Rykaczewski, D. G. Sarantites, and J. X. Saladin, D. Shapira, G. N. Sylvan, S. L. Tabor, K. S. Toth, W. Weintraub, D. F. Winchell, V. Q. Wood, R. Wyss, and C. H. Yu, *Phys. Rev. C* **58**, R3037 (1998).
- [66] N. Mărginean, D. Bucurescu, C. Rossi Alvarez, C. A. Ur, Y. Sun, D. Bazzacco, S. Lunardi, G. de Angelis, M. Axiotis, E. Farnea, A. Gadea, M. Ionescu-Bujor, A. Iordăchescu, W. Krolas, Th. Kröll, S. M. Lenzi, T. Martinez, R. Menegazzo, D. R. Napoli, P. Pavan, Zs. Podolyak, M. De Poli, B. Quintana, and P. Spolaore, *Phys. Rev. C* **69**, 054301 (2004).
- [67] H. Mach, S. Ćwiok, W. Nazarewicz, B. Fogelberg, M. Moszyński, J. Winger, and R. L. Gill, *Phys. Rev. C* **42**, R811 (1990).
- [68] D. J. Horen, R. L. Auble, G. R. Satchler, J. R. Beene, I. Y. Lee, C. Y. Wu, D. Cline, M. Devlin, R. Ibbotson, and M. W. Simon, *Phys. Rev. C* **48**, R2131 (1993).
- [69] P. Campbell, H. L. Thayer, J. Billowes, P. Dendooven, K. T. Flanagan, D. H. Forest, J. A. R. Griffith, J. Huikari, A. Jokinen, R. Moore, A. Nieminen, G. Tungate, S. Zemlyanoi, and J. Äystö, *Phys. Rev. Lett.* **89**, 082501 (2002).
- [70] G. Kumbartzki, N. Benczer-Koller, J. Holden, G. Jakob, T. J. Mertzimekis, M. J. Taylor, K. H. Speidel, R. Ernst, A. E. Stuchbery, C. W. Beausang, and R. Krücken, *Phys. Lett.* **B562**, 193 (2003).
- [71] H. Mach, G. Molnár, S. W. Yates, R. L. Gill, A. Aprahamian, and R. A. Meyer, *Phys. Rev. C* **37**, 254 (1988).
- [72] K. Heyde, E. D. Kirchuk, and P. Federman, *Phys. Rev. C* **38**, 984 (1988).
- [73] J. K. Hwang, A. V. Ramayya, J. H. Hamilton, J. O. Rasmussen, Y. X. Luo, D. Fong, K. Li, C. Goodin, S. J. Zhu, S. C. Wu, M. A. Stoyer, R. Donangelo, X.-R. Zhu, H. Sagawa, *Phys. Rev. C* **74**, 017303 (2006).
- [74] J. K. Hwang, A. V. Ramayya, J. H. Hamilton, Y. X. Luo, A. V. Daniel, G. M. Ter-Akopian, J. D. Cole, and S. J. Zhu, *Phys. Rev. C* **73**, 044316 (2006).
- [75] H. Mach, M. Moszyński, R. L. Gill, G. Molnár, F. K. Wohn, J. A. Winger, and J. C. Hill, *Phys. Rev. C* **41**, 350 (1990).
- [76] M. Bernas, C. Engelmann, P. Armbruster, S. Czajkowski, F. Ameil, C. Böckstiegel, P. Dessagne, C. Donzaud, H. Geissel, A. Heinz, Z. Janas, C. Kozhuharov, Ch. Miehé, G. Münzenberg, M. Pfützner, W. Schwab, C. Stéphan, K. Sümmerer, L. Tassan-Got, and B. Voss, *Phys. Lett. B* **415**, 111 (1997).
- [77] R. Julin, *Physica Scripta* **T56**, 151 (1995).
- [78] A. N. Andreyev, M. Huyse, P. Van Duppen, L. Weissman, D. Ackermann, J. Gerl, F. P. Heßberger, S. Hofmann, A. Kleinbohl, G. Münzenberg, S. Reshitko, C. Schlegel, H. Schaffner, P. Cagarda, M. Matos, S. Saro, A. Keenan, C. Moore, C. D. O’Leary, R. D. Page, M. Taylor, H. Kettunen, M. Leino, A. Lavrentiev, R. Wyss, and K. Heyde, *Nature* **405**, 430 (2000).
- [79] A. N. Andreyev, M. Huyse, P. V. Duppen, L. Weissman, D. Ackermann, J. Gerl, F. P. Heßberger, S. Hofmann, A. Kleinbohl, G. Münzenberg, S. Reshitko, C. Schlegel, H. Schaffner, P. Cagarda, M. Matos, S. Saro, A. Keenan, C. J. Moore, C. D. O’Leary, R. D. Page, M. J. Taylor, H. Kettunen, M. Leino, A. Lavrentiev, R. Wyss, and K. Heyde, *Nucl. Phys. A* **682**, 482c (2001).
- [80] A. N. Andreyev, M. Huyse, P. Van Duppen, J. F. C. Cocks, K. Helariutta, H. Kettunen, P. Kuusiniemi, M. Leino, W. H. Trzaska, K. Eskola, and R. Wyss, *Phys. Rev. Lett.* **82**, 1819 (1999).
- [81] T. Lesinski, K. Bennaceur, T. Duguet, and J. Meyer, *Phys. Rev. C* **74**, 044315 (2006).
- [82] D. Davesne, M. Martini, K. Bennaceur, and J. Meyer, *Phys. Rev. C* **80**, 024314 (2009).